JACS
JOURNAL OF THE AMERICAN CHEMICAL SOCIETY
Article
Cite This: J. Am. Chem. Soc. 2018, 140, 5457−5473
pubs.acs.org/JACS

Metal Composition and Polyethylenimine Doping Capacity Effects on Semiconducting Metal Oxide−Polymer Blend Charge Transport

Wei Huang,[†,‡] Peijun Guo,[∥] Li Zeng,[§] Ran Li,[∥] Binghao Wang,[†] Gang Wang,[†] Xinan Zhang,[†] Robert P. H. Chang,[∥] Junsheng Yu,[‡] Michael J. Bedzyk,[*,∥,§] Tobin J. Marks,[*,†] and Antonio Facchetti[*,†,⊥]

[†]Department of Chemistry and the Materials Research Center, Northwestern University, 2145 Sheridan Road, Evanston, Illinois 60208, United States

[‡]State Key Laboratory of Electronic Thin Films and Integrated Devices, School of Optoelectronic Information, University of Electronic Science and Technology of China (UESTC), Chengdu 610054, China

[∥]Department of Materials Science and Engineering and the Materials Research Center, Northwestern University, 2220 Campus Drive, Evanston, Illinois 60208, United States

[§]Applied Physics Program and the Materials Research Center, Northwestern University, 2220 Campus Drive, Evanston, Illinois 60208, United States

[⊥]Flexterra Inc., 8025 Lamon Avenue, Skokie, Illinois 60077, United States

Supporting Information

ABSTRACT: Charge transport and film microstructure evolution are investigated in a series of polyethylenimine (PEI)-doped (0.0−6.0 wt%) amorphous metal oxide (MO) semiconductor thin film blends. Here, PEI doping generality is broadened from binary In_2O_3 to ternary (e.g., In+Zn in IZO, In+Ga in IGO) and quaternary (e.g., In+Zn+Ga in IGZO) systems, demonstrating the universality of this approach for polymer electron doping of MO matrices. Systematic comparison of the effects of various metal ions on the electronic transport and film microstructure of these blends are investigated by combined thin-film transistor (TFT) response, AFM, XPS, XRD, X-ray reflectivity, and cross-sectional TEM. Morphological analysis reveals that layered MO film microstructures predominate in PEI-In_2O_3, but become less distinct in IGO and are not detectable in IZO and IGZO. TFT charge transport measurements indicate a general coincidence of a peak in carrier mobility (μ_{peak}) and overall TFT performance at optimal PEI doping concentrations. Optimal PEI loadings that yield μ_{peak} values depend not only on the MO elemental composition but also, equally important, on the metal atomic ratios. By investigating the relationship between the MO energy levels and PEI doping by UPS, it is concluded that the efficiency of PEI electron-donation is highly dependent on the metal oxide matrix work function in cases where film morphology is optimal, as in the IGO compositions. The results of this investigation demonstrate the broad generality and efficacy of PEI electron doping applied to electronically functional metal oxide systems and that the resulting film microstructure, morphology, and energy level modifications are all vital to understanding charge transport in these amorphous oxide blends.

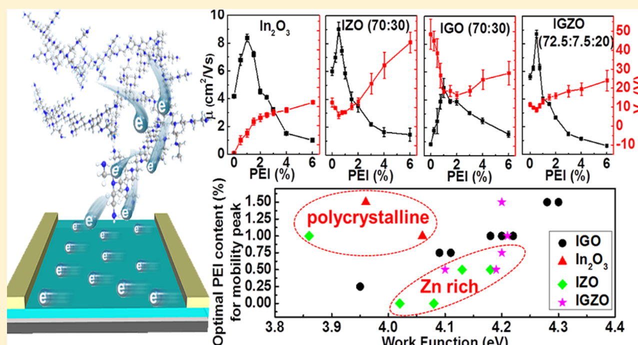

INTRODUCTION

Post-transition metal oxides have attracted intense research interest due to their high electrical conductivity/carrier mobility even in the amorphous state and excellent optical transparency in the visible region.[1−7] Furthermore, high-performance metal oxide semiconductors can be fabricated at low temperatures via both vacuum and solution processes.[8−12] As a result, thin-film transistors (TFTs) with good mechanical flexibility, high electron mobility, and excellent optical transparency can be fabricated, and can be used for advanced flat panel displays and a diversity of unconventional electronic products.[13−16] Nowadays, state-of-the-art metal oxide films, which are usually fabricated by physical or chemical vacuum processes such as radio frequency sputtering or chemical vapor deposition, have been commercialized as transparent conducting/semiconducting elements[17] and in high-resolution displays.[18] However, these processes are expensive due to the high capital cost of vacuum equipment, high power consumption, and ultralong fabrication times due to the use of multiple photolithographic steps.[4] Therefore, the development of high-performance and environmentally/thermally stable metal oxide films by solution

Received: January 31, 2018
Published: April 4, 2018

Downloaded via NORTHWESTERN UNIV on July 6, 2018 at 17:09:02 (UTC).
See https://pubs.acs.org/sharingguidelines for options on how to legitimately share published articles.

ACS Publications © 2018 American Chemical Society

processing has the potential to address the above challenges and enable low-cost oxide electronics manufacturing.[19−24]

The most heavily investigated metal oxide as both conductor and semiconductor is indium oxide (In_2O_3 or IO), since the extensive 5s orbital overlap leads to a broad conduction band with high electron mobility even in the amorphous state, with a large band gap which ensures optical transparency.[25−27] The conventional strategy to achieve optimal conductivity or semiconducting transport in In_2O_3 is to chemically dope the In_2O_3 with at least one secondary ion such as tin, resulting in the extensively used transparent conductor ITO (indium−tin−oxide),[28−30] and gallium + zinc, resulting in the high-mobility transparent semiconductor IGZO (indium−gallium−zinc−oxide).[31−34] In ITO, the role of Sn is to enhance the carrier density by donating high densities of free electrons to the lattice as a consequence of the oxidation state difference between In^{3+} and Sn^{4+}.[35] In IGZO, the presence of both metals is essential to achieve good semiconductor performance, since poor control of the carrier concentration in pure In_2O_3 makes it difficult to control the TFT off-current (I_{OFF}) and threshold voltage (V_T).[29,36−38] To some degree, adjusting the In_2O_3 thickness and post-annealing conditions can reduce the carrier concentration in In_2O_3. However, thin and low-temperature (<250 °C) annealed In_2O_3 films are unsuitable for achieving high-mobility and stable TFT characteristics.[39] Moreover, In_2O_3 tends to crystallize at relatively low temperatures to form polycrystalline films, which is not desirable for mechanical flexibility and film electrical/morphological uniformity over large areas.[40,41] In IGZO, Ga forms stronger chemical bonds to oxygen and suppresses the formation of oxygen deficiencies and free electrons, serving the role of a "stabilizer" or "suppressor".[33,36,42] The role of Zn is less clear but it is believed to stabilize the amorphous state, and is known in glass science as a "network modifier".[43−45]

Regarding semiconducting applications, we recently reported that the addition of certain quantities (x wt%) of electrically insulating polymers such as poly(4-vinylphenol) (PVP) or polyethylenimine (PEI) to In_2O_3 processing solutions yields amorphous oxide-polymer films with excellent semiconducting properties.[46−48] While the effects of PVP appear to simply amorphosize In_2O_3, which stabilizes the electron transport at the expense of the electron mobility ($\mu_{In_2O_3\ matrix} \approx 3.2$ cm^2/(V·s), $\mu_{In_2O_3+5\ wt\%\ PVP} \approx 2.1$ cm^2/(V·s)), PEI operates differently since we demonstrated that the electron-rich nitrogen centers can also act as electron donors to In_2O_3. The results are amorphous PEI+In_2O_3 blends exhibiting even greater electron mobilities ($\mu_{In_2O_3+PEI}$ as high as 9 cm^2/(V·s)) than the pristine oxide ($\mu_{In_2O_3} \approx 4$ cm^2/(V·s)) by carefully controlling the doping concentration of PEI at 1.0−1.5 wt%.[47] Charge transport in these TFTs was rationalized by the interplay of the following effects: (1) *Charge transfer*. PEI donates electrons, thus can enhance the carrier concentration and consequently both on-current (I_{ON}) and I_{OFF}. (2) *Charge scattering*. PEI introduces film contaminants, creating charge traps and depressing transport. (3) *Microstructure*. Grazing incidence X-ray diffraction (GIXRD) experiments clearly revealed that the film amorphous fraction increases with increasing the PEI content while X-ray reflectivity (XRR) indicate layered structure formation. (4) *Film density*. The oxide volume fraction in the TFT channel decreases as the PEI content increases, thus enhancing the insulating portion of the film.

In view of the remarkable results achieved with In_2O_3, it is intriguing to ask whether this approach is extendable to other metal oxide compositions, whether polymer doping efficiency is different when different metals or metal combinations are employed, what is the effect of polymer loading with MO composition, and whether and how charge transport and film microstructure are affected when the metal content varies. In this contribution, we prepare and investigate polycrystalline/amorphous ternary/quaternary metal oxide semiconductors [indium−zinc−oxide (IZO), indium−gallium−oxide (IGO), and indium−gallium−zinc−oxide (IGZO)] doped with varying PEI concentrations and explore the combined effects of PEI doping level and secondary metal ions with respect to pristine and PEI-doped In_2O_3 compositions. Note that previous work did not address any questions about using amorphous matrices, did not discuss whether other MO compositions would behave similarly, nor correlated doping capacity with the electronic structure/work function (WF) of the metal oxide and how these parameters change with PEI addition. In this manuscript, most of the other MO starting matrices are amorphous, thereby providing an opportunity to elucidate how PEI affects transport via lattice disruption versus other effects. Specifically, we compare and contrast the film microstructural properties of PEI-doped IZO, IGO, and IGZO vs In_2O_3 using atomic force microscopy (AFM), X-ray photoelectron spectroscopy (XPS), and GIXRD, followed by XRR and cross-section transmission electron microscopy (TEM). XRD and XPS indicate that, in sharp contrast to In_2O_3, when a secondary element is present, minimal variations are detected in the overall amorphous structure and oxygen lattice content upon PEI addition. However, AFM, XRR, and cross-section TEM demonstrate substantial variations in the film morphological properties. Finally, we demonstrate that tuning the WF of selected MO films by varying the metal (Ga or Zn) molar ratios, strongly influences the doping capacity of PEI, and certain MOs do not exhibit mobility peaks. Thus, this paper provides a complete, consistent, and insightful description of PEI electron-doping capacity and insights into the mechanism of PEI doping in metal oxide semiconductors and their energy levels.

EXPERIMENTAL SECTION

Precursor solutions. For the PEI-doped metal oxide precursor preparation, each metal nitrate salt (354.8 mg of $In(NO_3)_3{\cdot}xH_2O$; 297.2 mg of $Zn(NO_3)_2{\cdot}xH_2O$; 399.6 mg of $Ga(NO_3)_3{\cdot}xH_2O$; all from Sigma-Aldrich, 99.999% trace metals basis) was dissolved in 10 mL high-purity deionized (DI) water. After stirring for about 1 h, the precursor solutions were combined by micropipet to the desired molar ratios (for IZO, In:Zn = 96:4, 90:10, 80:20, and 70:30; for IGO, In:Ga = 96:4, 85:15, 70:30 and 60:40; for IGZO, In:Ga:Zn = 80:10:10, 70:10:20, 70:15:15, 70:20:10, 72.5:7.5:20, 60:20:20) and stirred. PEI (Sigma-Aldrich, average $M_w \approx 25\,000$ by LS, average $M_n \approx 10\,000$ by GPC, branched) was also dissolved in DI water to achieve concentrations of 20 mg/mL. After these solutions were stirred for at least 6 h, the PEI solution was added to the metal oxide precursor solution to achieve the desired polymer weight fraction indicated here as MO:x wt% PEI [MO = IO, IZO, IGO, and IGZO; x = 0.0−6.0]. After addition, the MO:polymer precursor solutions were stirred at least for 8 h before use.

For the PVP-doped MO precursor preparation, each metal nitrate salt (354.8 mg of $In(NO_3)_3{\cdot}xH_2O$; 297.2 mg of $Zn(NO_3)_2{\cdot}xH_2O$; 399.6 mg of $Ga(NO_3)_3{\cdot}xH_2O$; all from Sigma-Aldrich, 99.999% trace metals basis) was dissolved in 14 mL of 2-methoxyethanol. After stirring for about 1 h, the precursor solutions were combined by micropipet in the desired molar ratios (for IZO, In:Zn = 70:30; for IGO, In:Ga = 70:30; for IGZO, In:Ga:Zn = 72.5:7.5:20) and stirred.

DOI: 10.1021/jacs.8b01252
J. Am. Chem. Soc. 2018, 140, 5457−5473

PVP (Sigma-Aldrich, $M_w \approx 25\,000$) was also dissolved in 2-methoxyethanol to achieve concentrations of 14 mg/mL. Note, in contrast to PEI, PVP does not dissolve in water. After these solutions were stirred for at least 6 h, the PVP solution was added to the metal oxide precursor solution to achieve the desired polymer weight fraction indicated here as MO:*x* wt% PVP [MO = IZO, IGO, and IGZO; x = 0.0–6.0]. After addition, the MO:polymer precursor solutions were stirred at least for 8 h before use.

Transistor Fabrication and Electrical Characterization. *Unpatterned TFTs.* The chemical structure of PEI and a schematic of a PEI-doped film and transistor fabrication processes are shown in Figure S1. n^{++}-Si wafers with 300 nm thermally grown SiO_2 were used as the gate electrode and dielectric layer, respectively. Before spin-coating, these substrates were cleaned ultrasonically in isopropyl alcohol and with an O_2 plasma. Next, the MO:polymer precursor solutions were spin-coated on the substrates at 3000 rpm for 20s, and then annealed on a hot plate at a temperature (T_{ann}) at 200, 225, 250, or 300 °C for 30 min. This process was repeated three times to achieve the desired thickness of 10–12 nm. Finally, 40 nm Al source drain electrodes were thermally evaporated to form a channel length of 100 μm, and channel width of 1000 μm.

Patterned TFTs. For patterned IZO(70:30, 300 °C), IGO(70:30, 300 °C), and IGZO(72.5:7.5:20, 300 °C) TFTs, an identical process was carried out for the MO:PEI film deposition, which was then patterned before source-drain Al deposition. Semiconductor layer patterning was achieved by spin-coating the S1813 photoresist (5000 rpm for 30 s, 1.2 μm), which was annealed at 115 °C and then exposed to UV light (Inpro Tech., F300S) for 2 s through a photo mask. Next, the S1813 film was developed by soaking in MF319 for 30 s, and the films were rinsed with water and dried by a nitrogen flow. The exposed oxide film was then etched in oxalic acid (3.6% w/v) for 20 s, and rinsed with water. The remaining S1813 film was dissolved in acetone and the samples were rinsed with ethanol. Finally, the samples were further annealed at 300 °C for 5 min to remove any residual solvent.

For both type of devices, TFT characterization was performed under ambient in dark on a custom probe station using an Agilent 1500 semiconductor parameter analyzer. The electron mobility (μ) was calculated in the saturation region using eq 1, where I_D is the drain current, C_i is the capacitance per unit area of the dielectric layer, and V_G is gate voltage. W and L are channel width and length, respectively.

$$I_D = \frac{WC_i}{2L}\mu(V_G - V_T)^2 \tag{1}$$

Oxide Film Characterization. AFM film topographies were imaged with a Veeco Demension Icon scanning Probe Microscope using tapping mode. GIXRD and XRR measurements were carried out with a Rigaku SmartLab Thin-film Diffraction Workstation using a high-intensity 9 kW copper rotating anode X-ray source which is coupled to a multilayer optic. XPS was performed on Thermo Scientific ESCALAB 250Xi at a base pressure of 2×10^{-9} mbar. UPS spectra were recorded also on Thermo Scientific ESCALAB 250Xi at a base pressure of 2×10^{-8} mbar, using the He I line at $h\nu$ = 21.21 eV with samples biased at −5 V. Spectra were obtained after the surface of the film was etched for about 2 nm to minimize surface contamination. Note for UPS measurements, all films were fabricated on conducting ITO glass. Cross-sectional TEM measurements were performed using a JEOL JEM-2100F instrument, with samples prepared directly from films grown on Si/SiO_2 substrates (the same as used to fabricate actual devices) by utilizing FIB techniques (FEI Helios NanoLab 600). A thin Au layer was deposited on the sample to protect from damage during the FIB processing. Cross-sectional TEM EDS measurements were performed using Hitachi HD-2300 Dual EDS Cryo STEM, which has ultrasensitive dual-EDS capability.

RESULTS AND DISCUSSION

PEI-Doped Metal Oxide Blend Film Fabrication and Charge Transport Characteristics. To evaluate PEI doping effects on IZO, IGO, and IGZO versus In_2O_3 transport characteristics, TFTs fabricated with MO blends (for IZO, In:Zn = 70:30; for IGO, In:Ga = 70:30; for IGZO, In:Ga:Zn = 72.5:7.5:20 mol ratios) having the same PEI doping concentration range (0.0–6.0 wt%) were first investigated. Briefly, all films were fabricated by spin-coating aqueous PEI–metal oxide precursor solutions on n^{++}-Si wafers with a 300 nm thermally grown SiO_2 layer, followed by thermal annealing on a hot plate at a temperature (T_{ann}) of 300 °C. Note that for each composition this spin-coating and annealing process was repeated 3 times to achieve the desired MO film thickness of 10–12 nm. For TFT fabrication, note that the n^{++}-Si and SiO_2 function as the gate electrode and dielectric, respectively, and the device is completed by thermal evaporation through a shadow mask of 40 nm thick Al source/drain electrodes (channel length, L = 100 μm; channel width, W = 1 mm).

Bimetallic Systems. Figures 1, S2, and S3 show representative transfer plots for the TFTs based on these compositions; data are compiled in Table 1. As shown in

Table 1. Performance Metrics for Transistors Based on IZO (In:Zn = 70:30), IGO (In:Ga = 70:30), IGZO (In:Ga:Zn = 75:7.5:20), and In_2O_3 Blends with the Indicated PEI Concentrations, Annealed at T_{ann} = 300 °C[a]

MO matrix	TFT	PEI concentration [wt%] 0	0.25	0.5	0.75	1	1.5	2	3	4	6
In_2O_3[b]	μ [cm²/Vs]	4.18±0.11		6.78±0.39		8.37±0.28	7.20±0.20	4.52±0.18	3.22±0.13	1.51±0.05	1.01±0.02
	V_T [V]	-14.6±1.1		-7.6±2.4		-3.9±2.1	2.1±1.8	4.2±2.0	6.8±1.6	8.2±1.4	12.3±0.8
	I_{ON}/I_{OFF}	10^4		10^6		10^6~10^7	10^7	10^6~10^7	10^6~10^7	10^6~10^7	10^6
IZO	μ [cm²/Vs]	6.01±0.29	7.00±0.33	9.03±0.49	7.47±0.29	5.87±0.42	4±0.52	3.51±0.44	2.2±0.14	1.65±0.32	1.46±0.46
	V_T [V]	12.5±2.3	9.7±0.7	5.8±1.6	7.2±1.0	7.5±0.9	10.4±1.5	13.0±2.0	22.4±5.43	32.0±6.8	44.0±5.4
	I_{ON}/I_{OFF}	10^7	10^7	10^7	10^7	10^7	10^7	10^6~10^7	10^6~10^7	10^6~10^7	10^6
IGO	μ [cm²/Vs]	0.82±0.02	1.8±0.23	2.47±0.90	3.88±0.53	4.85±0.68	3.90±0.15	3.87±0.25	3.05±0.11	2.50±0.20	1.54±0.22
	V_T [V]	48.6±7.9	45.1±5.1	38.7±7.5	27.0±6.5	18.7±1.1	18.9±2.9	16.7±1.7	18.9±2.6	24.8±5.1	28.2±6.1
	I_{ON}/I_{OFF}	10^5~10^6	10^6	10^6~10^7	10^6~10^7	10^6~10^7	10^6~10^7	10^6~10^7	10^6~10^7	10^6~10^7	10^6~10^7
IGZO	μ [cm²/Vs]	5.63±0.19	6.24±0.16	8.71±0.26	6.30±0.20	4.06±0.11	3.65±0.12	2.67±0.08	1.48±0.12	1.14±0.05	0.63±0.09
	V_T [V]	11.3±1.1	9.7±0.7	8.5±1.2	10.7±1.1	13±1.4	15.1±1.5	16.0±1.4	18.4±3.0	19.5±3.3	24.0±5.5
	I_{ON}/I_{OFF}	10^7	10^7	10^7	10^7	10^7	10^7	10^6~10^7	10^6~10^7	10^6	10^6

[a]Value reported for each device is the average of that data reported for a minimum of 10 devices. [b]From ref 47. Note, for In_2O_3, T_{ann} = 250 °C.

DOI: 10.1021/jacs.8b01252
J. Am. Chem. Soc. 2018, 140, 5457–5473

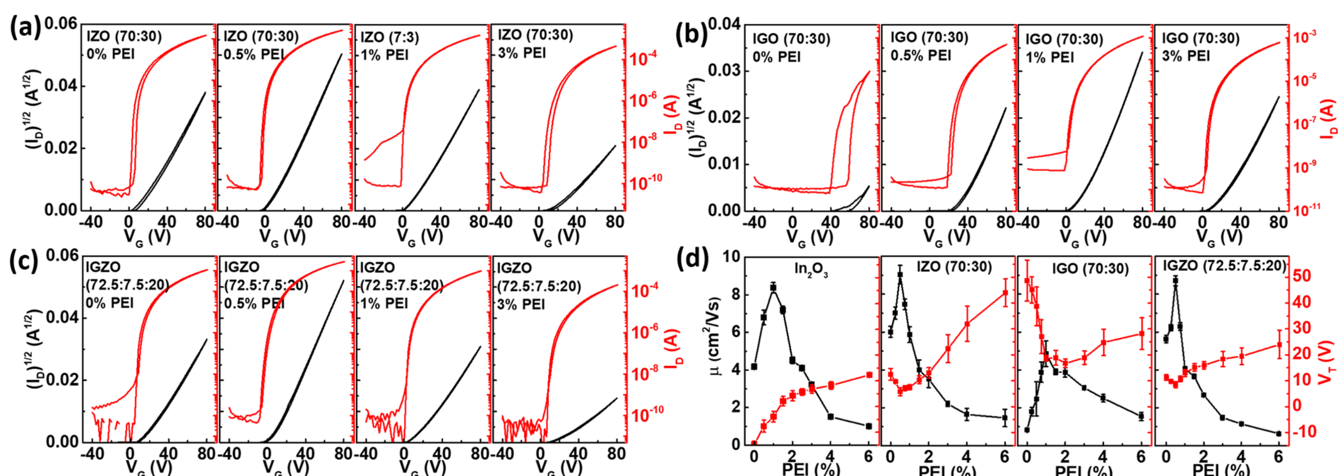

Figure 1. Representative TFT transfer characteristics for the indicated films: (a) IZO:*x* wt% PEI, (b) IGO: *x* wt% PEI, and (c) IGZO: *x* wt% PEI TFTs. V_D = +80 V. (d) TFT mobility and threshold voltage for In_2O_3:*x* wt% PEI (250 °C), IZO:*x* wt% PEI, IGO:*x* wt% PEI, and IGZO: *x* wt% PEI, as a function of the polymer concentration. T_{ann} = 300 °C.

Figures 1a and S2, for IZO(70:30):*x* wt% PEI-based transistors, the on-current (I_{ON}) first increases from 1.44 × 10^{-3} A (0.0 wt % PEI) to 2.54 × 10^{-3} A (0.5 wt% PEI), then slowly falls to 7.26 × 10^{-4} A (2.0 wt% PEI). When the concentration of PEI is greater than 3.0 wt%, I_{ON} decreases substantially (1.88 × 10^{-4} A at 4.0 wt% PEI doping, 9.43 × 10^{-5} A at 6.0 wt% PEI doping). The turn-on voltage (V_{ON}) also exhibits an interesting trend with an initial negative shift from 0.0 V for 0.0 wt% PEI to −8.0 V for 0.5 wt% PEI, followed by a positive shift in the PEI doping range 0.75−6.0 wt%.

Especially for 4.0 and 6.0 wt% PEI doping, large V_{ON} values of +22.0 V and +36.0 V, respectively, are observed. On the other hand, I_{OFF} shows no substantial variations (10^{-10}−10^{-9} A) across the range of PEI contents since solution processed IZO films (In:Zn molar ratio = 70:30) exhibit an intrinsic low carrier concentration, unlike typical In_2O_3 films. Furthermore, *I*−*V* hysteresis in the transfer plots has a two-stage evolution, depending on the PEI concentration. First, the hysteresis minimizes to <1.0 V when the PEI concentration is increased from 0.0 wt% to 0.5−1.5 wt% (4.0 V for 0.0 wt% PEI), then, increases to ∼4.0 V when the PEI concentration is >2.0 wt%. *I*−*V* hysteresis (clockwise between forward and backward sweep) indicates electron charge trapping in the channel layer.[49,50]

IGO-based transistors exhibit much steeper variations in the transfer curves when increasing the PEI content (Figures 1b and S3). Pristine IGO (In:Ga = 70:30) films exhibit poor transistor behavior, with a small I_{ON} of 2.86 × 10^{-5} A, a large V_{ON} of +38.0 V, and a considerable *I*−*V* hysteresis of >15.0 V. It is known that for IGO films solution-processed at low temperatures (<400 °C), especially when the Ga content is greater than 10 wt%, oxygen vacancies which act as an electron carrier source will be suppressed, thus resulting in inferior electrical performance.[51] However, upon PEI addition I_{ON} increases from 2.86 × 10^{-5} to 4.90 × 10^{-4} A (0.5 wt% PEI) and 1.16 × 10^{-3} A (1.0 wt% PEI), with the latter almost 100× greater than that in IGO without PEI doping. Higher PEI doping concentrations (>1.0 wt%) decrease I_{ON} (8.27 × 10^{-4} A for 2 wt% PEI and 4.77 × 10^{-4} A for 4 wt% PEI), albeit to values larger than that of the PEI-free IGO transistors. Equally important, V_{ON} also shifts to either negative (−2.0 to 0.0 V for 1.0−3.0 wt% PEI) or positive (+2 V for 4 wt% PEI) values closer to zero volts. The *I*−*V* hysteresis in PEI-doped IGO transistors also decreases (<8.0 V) compared to the neat IGO devices. Especially for PEI doping concentrations of ∼1 wt%, the hysteresis falls to less than 1.0 V. Similarly to IZO, the I_{OFF} values of IGO TFTs show negligible variations with the PEI content and remain in the range of 10^{-10}−10^{-9} A.

Trimetallic Systems. IGZO (In:Ga:Zn = 72.5:7.5:20)-based transistors exhibit electrical parameter trends as a function of PEI concentration which are qualitatively similar to those of the bimetallic systems (I_{ON}, V_T, and I_{OFF}; Figures 1c and S4). Thus, I_{ON} first increases from 1.10 × 10^{-3} A (0.0 wt% PEI) to 2.72 × 10^{-3} A (0.5 wt% PEI), then falls to 6.92 × 10^{-4} A (2.0 wt% PEI), 1.48 × 10^{-4} (4.0 wt% PEI), and 5.94 × 10^{-5} A (6.0 wt% PEI). Simultaneously, V_{ON} shifts first from +4.0 V (0.0 wt% PEI) to −10.0 V (0.5 wt% PEI), then positive shifts from −2.0 V to +18.0 V are obtained in the PEI doping range of 0.75−6.0 wt%. For these increases in PEI content, I_{OFF} remains in the range of ∼10^{-10} A, similar to that in the aforementioned PEI-doped IZO- and IGO-based transistors.

From the transistor transfer curves, the current on/off ratio (I_{ON}/I_{OFF}), *μ*, and V_T can be extracted using known MOSFET models,[4,46] and all data are summarized in Table 1. Figure 1d presents *μ* and V_T plots as a function of the PEI content for all MO:*x* wt% PEI TFTs investigated here plus those of the devices based on the In_2O_3 control.[47] Remarkably, and similarly to In_2O_3:*x* wt% PEI TFTs and independent of the MO elemental composition, all *μ* values maximize over a narrow PEI content range. However, there are also interesting differences in these MO composite transport parameters versus those of the PEI-doped In_2O_3 devices. Compared to In_2O_3 where a maximum electron mobility, or mobility peak (μ_{peak}) of 8.37 ± 0.28 $cm^2/(V \cdot s)$ is achieved at 1.0 wt% PEI, the IZO and IGZO film mobilities maximize at 9.03 ± 0.49 and 8.71 ± 0.26 $cm^2/(V \cdot s)$, respectively, for a 0.5 wt% PEI loading (Figure 1d and Table 1).

Similar to In_2O_3, the μ_{peak} of IGO (4.85 ± 0.68 $cm^2/(V \cdot s)$) is obtained at 1.0 wt% PEI doping. The maximum mobility trend of MO:*x* wt% PEI composites reflect the characteristics of the starting MO matrices, and thus it is expected that IGO should underperform the other MOs because of the strong affinity of Ga for oxygen.[52,53] However, note also that a mobility for IGO (In:Ga = 70:30, 300 °C) as high as ∼4.9 $cm^2/(V \cdot s)$ is

DOI: 10.1021/jacs.8b01252
J. Am. Chem. Soc. 2018, 140, 5457−5473

unprecedented.[51,54] Furthermore, while the V_T values of In_2O_3:*x* wt% PEI monotonically increase (positive shift) with the PEI concentration (−14.6 ± 1.1 V for 0.0 wt% PEI, −3.9 ± 2.1 V for 1.0 wt% PEI, 12.3 ± 0.8 V for 6.0 wt% PEI), for all of other MO:*x* wt% PEI devices, V_T first decreases (Figure 1d) from +12.5 ± 2.3 V (neat IZO), + 48.6 ± 7.9 V (neat IGO), and +11.3 ± 1.1 V (neat IGZO), to +5.8 ± 1.6 V (0.5 wt% PEI-doped IZO), + 18.7 ± 1.1 V (1.0 wt% PEI-doped IGO), and +8.5 ± 1.2 V (0.5 wt% PEI-doped IGZO), respectively, and then increases to much larger values of +44.0 ± 5.4 V (6.0 wt% PEI-doped IZO), + 28.2 ± 6.1 V (6.0 wt% PEI-doped IGO), and +24.0 ± 5.5 V (6.0 wt% PEI-doped IGZO), respectively.

Finally, to exclude the possibility of mobility overestimation or artifacts in the TFT performance trends, due to the unpatterned semiconductor structure of our devices, selected TFTs with a patterned MO semiconducting layer were also fabricated and analyzed. As shown in Figure S8, the mobility and V_T trends are identical to those shown in Figure 1d (without patterning), with a mobility peak established at 0.5 wt % for IZO(70:30, 300 °C) and IGZO(72.5:7.5:20, 300 °C), and 1.0 wt% for IGO(70:30, 300 °C). We also note that the mobilities of these pattered devices are slightly larger, which is possibly due to the additional semiconductor film solvent treatment/thermal annealing associated to the patterning process. However, these data demonstrate that semiconductor patterning is not essential for underscoring the PEI effects in these devices and, equally important, that our PEI doping approach is fully compatible with conventional MO photolithographic processes.

Bias Stress Measurements and Control Experiments. Negative bias stability (NBS) and positive bias stability (PBS) evaluations were also carried out to examine the reliability of our PEI-doped metal oxide TFTs, considering implications for practical applications. Both positive and negative bias-stress tests for IZO(70:30, 300 °C), IGO(70:30, 300 °C), and IGZO(72.5:7.5:20, 300 °C) were performed and the results are collected in Figures S9−S11. Note that these tests were performed with the semiconductor channel directly exposed to the air without any passivation layer. Both IZO and IGZO devices without or with 0.5 wt% PEI doping (Figures S9 and S10) exhibit similar V_T shifts (−15 V to −18 V) when performing the NBS test (V_G = −30 V for 1000 s). This result indicates that PEI doping does not affect intrinsic stress characteristics of these devices. The neat and PEI-doped IGO TFTs stressed under the same conditions (Figure S11) exhibit a negligible and ∼−8 V V_T shift, respectively. The small V_T shifts of IGO TFTs under negative bias are likely due to the strong Ga−O bonds, which prevent desorption of O_2 and thus maintain the carrier concentration at very low levels during the stress experiment.[18] On the other hand, all IZO, IGO, and IGZO TFTs subjected to a PBS exhibit reduced V_T shifts when doped with the optimal PEI content. Thus, for IZO and IGZO TFTs stressed at V_G = +40 V for 1000 s, the V_T shift decreases from +16 V and +13 V (0.0 wt% PEI) to +7 V and +4 V (0.5 wt % PEI), respectively. Stressing IGO TFTs requires to use a much larger positive bias considering that the V_{ON} of these devices is close to +40 V. However, although stressed with a V_G = +80 V for 1000 s (Figure S11), these devices exhibit a V_T shift which decreases from +29 V (0.0 wt% PEI) to +14 V (1.0 wt% PEI). Thus, based on the NBS and PBS measurements, it is clear that the bias stress characteristics of PEI-doped TFTs are comparable to or even superior to those of the undoped devices, in agreement with the decreased charge trap concentrations.

Furthermore, we carried out control experiments by fabricating devices using PVP as dopant, a polymer which cannot readily donate electrons. For these polymer-MO blends, as reported previously for In_2O_3 TFTs,[46] we expect that the mobility should deteriorate as the polymer content increases. Figures S12−S14 report the transfer curves for PVP-doped IZO(70:30, 300 °C), IGO(70:30, 300 °C), and IGZO-(72.5:7.5:20, 300 °C) transistors. The results are fully consistent with the expectation that an insulating polymer without electron-donating atoms deteriorate device performance, with the mobility decreasing monotonically and V_T value shifting positively (Figure S15) as the PVP content increases. Note, in these experiments, the performance of the neat metal oxide based TFTs are not the same as those reported for the PEI doping experiments since a different solvent (2-methoxyethanol from PVP vs water for PEI) is used for the formulation, as indicated in the Experimental Section.

From the combined results presented above, it is clear that the electron-donating capabilities of PEI are essential for explaining the charge transport and performance parameter trends in the devices described so far. The above MO mobility trends and performance optimization metrics in our MO TFTs for 0.5−1.5 wt% PEI concentrations clearly argue that PEI has the capacity to transfer electrons to all of the present MO matrices, independent of the constituent metal(s) and intrinsic initial performance. As mentioned in the Introduction, the overall oxide TFT performance is a balance of several effects resulting from PEI addition. For very low and optimal PEI content, the added PEI fraction will create only a small amount of additional deep traps (*vide infra* XPS analysis), which are however prefilled by the electrons provided by the electron-donating nitrogen atoms of the PEI. Furthermore, the electrons provided by this small/optimal amount of PEI also fills shallow traps. These combined effects explain the reduced *I-V* hysteresis and the combination of enhanced I_{ON} values and mobilities. Interestingly, as shown in Figure 1d and Table 1, the V_T variations with wt% PEI in IZO, IGO, and IGZO compared to those in In_2O_3, featuring a V_T minimum or a monotonic V_T increase crossing 0.0 V, respectively, indicate that the principal mechanism by which PEI operates in modulating the transport parameters depends on the metal composition and microstructure of the initial MO matrices (*vide infra*). However, when the PEI content exceeds the optimal values, which is dependent on the MO matrix chemistry and microstructure, then the electron-donating capacity of PEI is insufficient to prevent TFT performance degradation due to considerable MO microstructure disruption (*vide infra* XRD analysis) and reduced content of the transporting fraction in the TFT channel.

Characterization of PEI-Doped Metal Oxide Films. To understand the MO TFT performance variations on combining PEI with Zn and/or Ga in In_2O_3-based TFTs, the morphology and microstructures of the metal oxide films were characterized in detail. Since from Figure 1d it is evident that most of the performance variations occur in the PEI doping concentration ranges of 0.0−3 wt%, morphological and microstructural analysis focused on this polymer content regime.

AFM was first utilized to characterize the surface morphology of the ∼10 nm thick oxide films. Recall that these films are obtained by successive spin-coating/annealing ∼3 nm thick layers three times. Figure 2 indicates that pristine In_2O_3 films

DOI: 10.1021/jacs.8b01252
J. Am. Chem. Soc. 2018, 140, 5457−5473

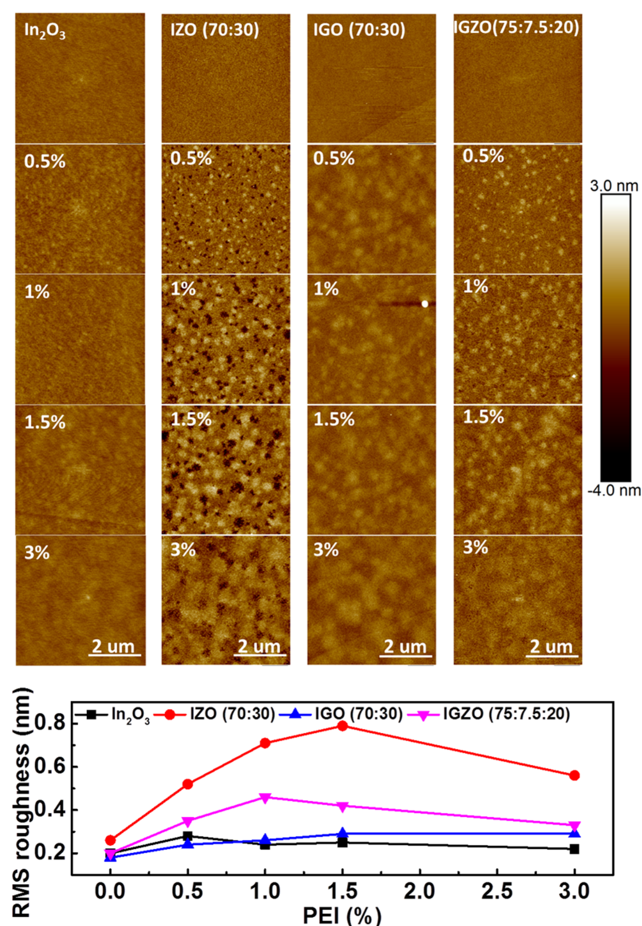

Figure 2. AFM height images and RMS roughness of the indicated metal oxide:x wt% PEI blend films as a function of PEI concentration. T_{ann} = 300 °C except for In_2O_3 (250 °C).

exhibit an RMS roughness (σ_{RMS}) of 0.20 nm, while after doping with PEI the In_2O_3 films become slightly rougher with a σ_{RMS} < 0.30 nm. PEI addition to IZO increases the surface roughness [σ_{RMS} (nm) = 0.26 (0.0 wt% PEI), 0.52 (0.5 wt% PEI), 0.71 (1 wt% PEI), 0.79 (1.5 wt% PEI)] by generating small pinholes having a depth of ∼1−2 nm, along with some protrusions with height of ∼1 nm. These features enlarge as the PEI concentration increases, from a diameter of 0.1−0.2 μm (0.5 wt% PEI) to 0.3−0.4 μm (1.0 wt% PEI) to 0.5−1 μm (3.0 wt% PEI). For PEI-doped IGO films only small protrusions with heights <1.0 nm are observed after PEI doping, and all the films remain quite smooth with a σ_{RMS} < 0.3 nm. Finally, IGZO film morphologies have features in between those of IZO and IGO films and exhibit a lower density of small pinholes (size <0.1 μm) than IZO, with σ_{RMS} ranging from 0.20 nm (0.0 wt% PEI) to 0.46 nm (1.0 wt% PEI). For identical PEI concentrations (0.5−1.0 wt%), the IGZO film RMS roughnesses are greater than those of IGO (0.35−0.46 nm vs 0.24−0.26 nm, respectively) but lower than those of IZO films (0.52−0.71 nm, Figure 2). From these data it appears that combining Zn-containing MO films with PEI significantly increases the roughness.

Additionally, it is important to understand whether pinhole and protrusion features originate from phase separation between the polymer and the MO matrix. Thus, smaller regions of the PEI:IZO films, which produce the rougher films in this MO series, were analyzed by high-resolution AFM (Figure S16). The data indicate that all the IZO films over a range of PEI concentrations show similar morphologies, with small "grains" of ∼50 nm diameter. Increasing the PEI content creates pinholes with depths of 1−2 nm and protrusions with heights of ∼1 nm. Interestingly, both these regions exhibit similar morphological features (see Figure S16 phase images), indicating that there is no newly introduced phase separation when doping with PEI.

It is known that rougher semiconducting surfaces, which typically correspond to greater densities of grain boundaries, are not ideal for in-plane charge transport in a TFT geometry.[4] Since incorporating Zn and PEI in In_2O_3 (IZO: x wt%PEI) and IGO (IGZO: x wt%PEI) greatly increases the film roughness versus the corresponding In_2O_3:PEI and IGO:PEI blends, especially when the PEI concentration increases to 1.0−1.5 wt %, charge transport is expected to degrade, which is in agreement with the TFT measurements in Figures 1, S2, and S4. In contrast, incorporating Ga into the PEI-doped In_2O_3 and IZO systems does not compromise film morphology, and thus the doping capacity and other intrinsic effects of PEI addition are more evident and extend to greater PEI contents, in agreement with the TFT characterization data above.

Next, XPS was employed to probe chemical environments in these PEI-doped metal oxide films.[55] First, the O 1s spectra were analyzed and deconvoluted (Figure S17) assuming (1) M-O-M lattice species occur at 529.8 ± 0.1 eV, (2) bulk and surface metal hydroxide (M-OH) species are at 531.1 ± 0.1 eV, and (3) weakly bound M-OR species such as H_2O or CO_2 are at 532.2 ± 0.1 eV. The evolution of O 1s peaks in PEI-doped In_2O_3, IZO, IGO, and IGZO films are summarized in Figure 3

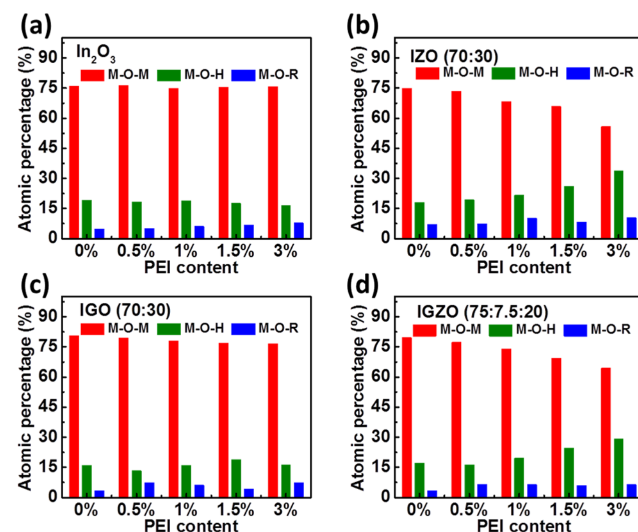

Figure 3. Summary of the relative M-O-M lattice, M-OH, and M-OR contents of metal oxide:x wt% PEI blend films with the indicated PEI concentrations. T_{ann} = 300 °C except for In_2O_3 (250 °C).

and Table S1. For the PEI-doped IZO films, the M-O-M peak decreases from 74.9% (0.0 wt% PEI) to 68.3% (1.0 wt% PEI), and to 55.8% (3.0 wt% PEI), while the peak corresponding to the metal hydroxide increases from 18.0% (0.0 wt% PEI) to 21.6% (1.0 wt% PEI), and to 33.8% (3.0 wt% PEI). There is also a slight increase of the M-OR peak intensity from 7.1% (0.0 wt% PEI) to 10.1% (1.0 wt% PEI), and to 10.4% (3.0 wt% PEI). However, the oxygen species content evolution with PEI doping is different for IGO. Only a small decrease in M-O-M

DOI: 10.1021/jacs.8b01252
J. Am. Chem. Soc. 2018, 140, 5457−5473

content from 80.7% to 76.6% can be observed in IGO when increasing the content of PEI from 0.0 wt% to 3.0 wt%, and upon PEI addition, the variation and the overall amount of M-OH and M-OR content are relatively small (13.3% → 18.9% for M-OH and 3.4% → 7.3% for M-OR; PEI = 0.0 wt% → 3.0 wt%).

Finally, the O 1s peak intensities in IGZO:x wt% PEI films exhibit identical variations with increasing PEI concentrations as IZO:x wt% PEI. Specifically, the M-O-M content decreases from 79.6% (0.0 wt% PEI) to 64.4% (3.0 wt% PEI), while the M-OH and the M-OR contents increase from 17.1% and 3.4% (0.0 wt% PEI) to 29.1% and 6.4% (3.0 wt% PEI), respectively. Oxygen species content variations in IGZO are not as dramatic as those in IZO:x wt% PEI, probably reflecting the synergetic effects of both Zn and Ga. Again, incorporating both Zn and PEI in In_2O_3 and IGO films results in a less favorable oxygen chemical environment with decreased M-O-M lattice content and increased M-OH fraction, which diminishes TFT mobility when the PEI content in IZO and IGZO is >1.0 wt%. However, small PEI additions below/at the optimal values (0.5−1.0 wt%) only minimally increases the M-OH content, while retaining a high M-O-M portion, thus enhancing the electron mobility.[47]

C 1s spectra were also analyzed to ensure PEI retention in all films after thermal annealing of the MO precursor, since in previous work the annealing temperature was 250 °C, and in this work, annealing temperatures as high as 300 °C are utilized.[47] As shown in Figure S18, the neat MO matrices exhibit traceable C peaks at 285.0 and 289.0 eV, which are due to environmental contamination. Importantly, all PEI-doped MO films show enhanced C 1s peak intensities as the PEI concentration increases (Figure S18) indicating that PEI chains remain largely intact in the film after 300 °C annealing. The C 1s signal in these metal oxide:PEI blends can be fit to three peaks at ∼285.0 eV, ∼ 287.0 eV and ∼289.0 eV. Peak at 285.0 eV can be assigned to C−C and C−N bonds, arguing that the PEI backbone survives in the film, while the C 1s peak at 287.0 eV is a C−O bond, and that at ∼289.0 eV is assignable to C=O, $C-NR_3^+$, and/or more complex C−O bonded species.[56−58] Moreover, the peak at ∼289.0 eV intensifies as the PEI concentration increases, suggesting that PEI has a significant reaction with O_2 during the annealing process.[59,60] The N 1s peak in IZO was also analyzed, as shown in Figure S19. In IZO without PEI doping, peaks at 404−405 eV are evident, indicating that small amounts of nitrate are not completely decomposed on annealing at 300 °C.[61] In doping with PEI, the peak at 404−405 eV slightly shifts to 403 eV, indicating decreased quantities of nitrate and an increase of positively charged ammonium N atoms.[58,60] Moreover, the peak at 398−399 eV, which is assigned to C−N bonds, and N partially coordinated to metal cations, intensifies, along with increasing PEI concentrations.[62,63] As Ga has a very strong Auger peak overlapped with the N 1s peak region, the N 1s peaks of PEI-doped IGO and IGZO cannot be discerned. These results suggest that PEI backbone fragments remain within the film even after 300 °C annealing and that partial oxidation/quaternization/coordination occurs during annealing. Thus, PEI is at the origin of the electron doping effect in these films and contributes to the enhanced electron mobility for optimal PEI contents, as shown in Figure 1d.

Microstructure Analysis of Polymer−Metal Oxide Blends. The above results primarily reveal that, when incorporating Zn and PEI into In_2O_3 (In:Zn = 70:30) and IGO (In:Ga:Zn = 72.5:7.5:20), the optimal PEI concentration to achieve μ_{peak} shifts to lower PEI contents, from 1 wt% in In_2O_3 and IGO to 0.5 wt% in IZO and IGZO. This reflects inferior surface morphology and reduced M-O-M lattice densification for excessive PEI contents (≥1.0 wt%) for MO compositions with Zn.

To obtain more insight into MO:x wt% PEI film microstructure trends, GIXRD, XRR, and CS-TEM measurements were made for all films having PEI doping concentration from 0.0−3.0 wt%, which span the mobility peak. As shown in Figure S20, independently of x wt% PEI, all of the new MO:x wt% PEI films are amorphous with the broad metal oxide amorphous peak centered at 2θ∼32°. The peak at ∼21° is from the substrate SiO_2 layer. While pristine In_2O_3 films are highly textured, the crystalline portion is strongly suppressed and monotonically decreases as the PEI concentration increases. This result is in agreement with previous observations using a different polymer dopant, poly(vinylphenol) (PVP),[46] albeit the PVP content in the In_2O_3: x wt% PVP blends was significantly larger, yielding completely amorphous In_2O_3 phases for x > 5 wt%.

Next, the MO films with/without PEI were examined by XRR. Since XRR is sensitive to the film electron density, layer spacing, and interfacial roughness, it can be utilized to examine film microstructural quality and structural evolution upon multilayer film deposition and PEI doping (Figure 4, and Table S2). Note that the XRR data were acquired on trilayer films deposited on Si/300 nm SiO_2 substrates fabricated by a three successive spin-coating/annealing steps (Figure S1). All XRR data were processed using Motofit.[64,65]

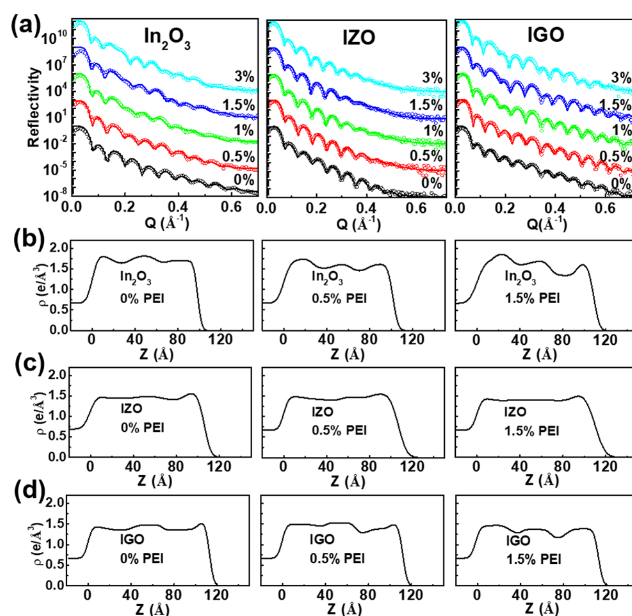

Figure 4. XRR plots and corresponding electron density profiles of In_2O_3, IZO, and IGO thin films with differing PEI concentrations. T_{ann} = 300 °C except for In_2O_3 (250 °C).

As shown in Figure 4a, while the XRR reflectivity oscillations of PEI-doped In_2O_3 films change substantially as the PEI content increases to >1.0 wt%, especially in the Q range of 0.1−0.3 Å^{-1}, those of IZO:x wt% PEI films remain similar throughout all compositions. Thus, the corresponding XRR-derived average electron density of PEI-doped In_2O_3 films decreases to a greater extent [1.70 e/Å^3 (neat In_2O_3); 1.62 e/Å^3

DOI: 10.1021/jacs.8b01252
J. Am. Chem. Soc. 2018, 140, 5457−5473

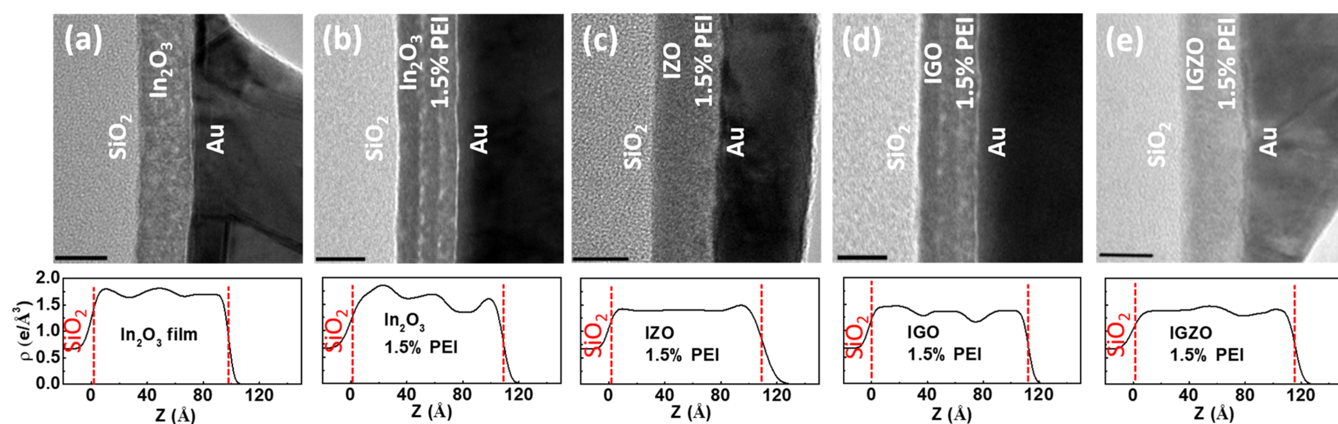

Figure 5. Cross-sectional TEM images of neat In_2O_3, 1.5 wt% PEI-doped In_2O_3, 1.5 wt% PEI-doped IZO(70:30), 1.5 wt% PEI-doped IGO(70:30), and 1.5 wt% PEI-doped IGZO(72.5:7.5:20), with their corresponding electron densities profiles fitted from XRR data. T_{ann} = 300 °C except for In_2O_3 (250 °C).

(1.5 wt% PEI); 1.53 e/Å^3 (3.0 wt% PEI)] than that of IZO:*x* wt % PEI films [1.45 e/Å^3 (0.0 wt% PEI); 1.40 e/Å^3 (1.5 wt% PEI); 1.36 e/Å^3 (3.0 wt% PEI) as the PEI content increases (Table S2). Moreover, consistent with the AFM data, the surface RMS roughness of IZO films increases from 0.49 nm (0.0 wt% PEI) to 0.72 nm (3.0 wt% PEI) as the PEI concentration increases, while the In_2O_3 films remain smooth (0.39−0.44 nm) regardless of PEI content. Finally, while PEI-doped In_2O_3 films reveal a clear periodic modulation of the electron density, evidence of a multilayer structure which becomes more evident as the PEI concentration increases (Figure 4b),[47] PEI-doped IZO films, on the other hand, are very uniform with no obvious multilayer structure (Figure 4c). For instance, while the layered structure of the 3.0 wt% PEI-doped In_2O_3 films is characterized by a progressive fall in electron density from the first (1.69 e/Å^3) to the second (1.61 e/Å^3) and third layer (1.40 e/Å^3), that of 3.0 wt% PEI-doped IZO exhibits only a slightly layered structure with a uniform density of ∼1.36 e/Å^3 (Figure S21).

On transitioning to IGO:*x* wt% PEI films, the reflectivity oscillations show less significant variations upon PEI addition versus those of In_2O_3:*x* wt% PEI films (Figure 4a). For these films the average electron density also decreases with increasing PEI concentration [from 1.43 e/Å^3 (0.0 wt% PEI) to 1.33 e/Å^3 (3.0 wt% PEI)] while the film roughness (0.33−0.36 nm) exhibits minimal variations (Table S2). However, for a given PEI content, unlike the uniform electron density observed for IZO:*x* wt% PEI films, the IGO film electron density evidences the formation of a layered structure similar to In_2O_3:*x* wt% PEI films (Figure 4d). For example, for the IGO:3.0 wt% PEI film, the electron density of the first layer is 1.38 e/Å^3, is higher than those of the second (1.33 e/Å^3) and third (1.27 e/Å^3) layers (Figure S21). Note however that layering is not as evident in IGO as in In_2O_3:*x* wt% PEI films. Finally, the XRR data for the PEI-doped IGZO films (Figure S21) demonstrate that increasing the PEI concentrations in IGZO from 0.0 wt% to 3.0 wt% decreases the average electron density from 1.48 e/Å^3 (0.0 wt% PEI) to 1.33 e/Å^3 (3.0 wt% PEI); however, both the film thicknesses (11.1−12.4 nm) and the surface roughness (0.38−0.45 nm) remain in a narrow range. The latter data are consistent with the AFM-derived RMS roughness values.

To further analyze the microstructures of these films, cross-sectional (CS) TEM data were acquired for 1.5 wt% PEI-doped In_2O_3, IZO, IGO and IGZO as well as neat In_2O_3 films (Figure 5). High-magnification TEM of 1.5 wt% PEI-doped In_2O_3 (Figure S22b) shows that the film consists mostly of an amorphous phase, in agreement with GIXRD measurements. The doped films were selected to corroborate and better understand the nature of the multilayer structure, when present. Figure 5a shows that the neat In_2O_3 film is relatively uniform along the vertical direction and features a mixture of lighter and darker regions. Note that the corresponding XRR-derived electron density profile shown in the bottom of the same figure confirms the quite uniform film density. Interestingly, higher magnification TEM indicates that the film is highly crystalline with lattice spacings visible (Figure S22a). In contrast, the CS TEM images of the In_2O_3:1.5 wt% PEI (Figure 5b) and IGO:1.5 wt% PEI (Figure 5d) films clearly show the formation of well-defined 3-layer structures. The first layer, which is closest to the SiO_2 substrate, displays the darkest gray scale, indicating the highest density among the three In_2O_3 layers. Note that the second (center) and third (on top, nearest to Au) layers become progressively lighter.

Similar trends are observed in corresponding electron density profile by XRR (Figure 5b and 5d, bottom), with the average electron density of the first layer greater than that of the second and third. Note, high-resolution CS-TEM of PEI-doped In_2O_3 (Figure S22b) and IGO (Figure S22d) films shows no obvious polymer-MO phase separation. Furthermore, detailed inspection of the electron density profile within each layer for the In_2O_3:1.5 wt% PEI films reveals that the area on top of each of the three layers is more dense than that at the bottom. Such gradients are evident in most of the MO films investigated here (see density profiles in Figures 4 and 5), and reveal well-defined multilayer structures such as in PEI-doped In_2O_3 and IGO or not such as in undoped In_2O_3 and PEI-doped IZO and IGZO (*vide infra*). It is known that when annealing/converting a metal oxide precursor to a MO film in air the uppermost surface of the film is typically denser since direct air exposure facilitates oxidation of the MO precursor and further facilitates film densification by release of gaseous byproducts.[66] Such phenomena were also observed in other solution processed metal oxides.[67,68] Higher PEI loadings enhance this effect not only for the third layer but, when present, for the other two layers as well, and is clearly seen for all 3 wt% PEI-doped MO samples (Figure S21).

Interestingly Zn addition to PEI-doped In_2O_3 and IGO films suppresses both the layering and enhances intralayer electron

DOI: 10.1021/jacs.8b01252
J. Am. Chem. Soc. 2018, 140, 5457−5473

density uniformity. On analyzing IZO:1.5 wt% PEI films (Figure 5c), no evidence of a layered structure is found. The AFM data indicate that the IZO, and to a far lesser degree the IGZO film surfaces are invariably rougher than those of the other metal oxide films, especially when incorporating PEI (Figure 2). This phenomenon is expected to enhance the film surface:volume ratio. This likely facilitates air diffusion into the films during the annealing step, promoting uniform precursor decomposition and promoting the formation of more uniform structures. As further confirmation, the CS-TEM of the 1.5 wt% PEI-doped IGZO film in Figure 5e reveals a morphology similar to that of 1.5 wt% doped IZO. Thus, analyzing the morphology evolution going from In_2O_3 and IGO to IZO and IGZO, respectively, clearly reveals that Zn incorporation affords relatively uniform electron density distributions, probably via forming rougher surfaces.

Finally, high-resolution CS-TEM of PEI-doped IZO film (Figure S22c) confirms that there is no obvious phase separation in the film. To study these aspects in more detail, energy-dispersive X-ray spectroscopy (EDS) measurements were carried out for the pristine In_2O_3 and MO:1.5 wt% PEI films (Figures S23−S27). Note EDS scans are conducted with a Hitachi HD-2300 Dual EDS Cryo STEM, which has a lower spatial resolution than that of JEOL JEM-2100F; thus the TEM figure is less clear than those in Figures 5 and S22. However, this TEM has ultrasensitive dual-EDS capability, which makes it a superior tool for elemental mapping. As shown in Figures S23 and S24, Indium is uniformly distributed throughout both the neat and 1.5 wt% PEI-doped In_2O_3 films. Carbon detection was also attempted, but the concentration is too low and the air-exposed sample absorbed large amounts of C species on the TEM sample surface. Thus, it is difficult to achieve a reasonable C mapping. However, these data further support a model in which PEI is evenly distributed throughout the film without macroscopic phase separation from the MO. Furthermore, elemental mapping of In, Zn, and Ga for all the remaining 1.5 wt% PEI-doped films indicates that all elements are uniformly distributed, demonstrating the formation of solid solutions (Figures S25−S27).

Charge Transport Evolution with PEI Doping. In our previous study of In_2O_3:*x* wt% PEI blends,[47] charge transport in the corresponding TFTs was explained in terms of the PEI electron doping capability, dramatic reduction of In_2O_3 matrix thin-film crystallinity, and formation of the unique trilayer film microstructure characterized by a dense first layer, in contact with the dielectric, enabling high mobility and the formation of more porous second/third layers controlling carrier density as in bilayer MO transistors. Thus, the layer adjacent to the dielectric offers an efficient channel for charge transport when the PEI content is low, prefilling traps and minimally disturbing charge transport, with any successive layer(s) controlling conductance, resulting in low I_{OFF} and suitable V_T. As a consequence, the V_T values of PEI-doped In_2O_3 TFTs always exhibit increasingly positive shifts with increasing PEI concentrations.

In all IZO:*x* wt% PEI and in IGZO:*x* wt% PEI films, when the PEI concentration is ≤1.0 wt%, there is negligible formation of distinct layered structures (Figure S21), a situation similar to that of undoped In_2O_3 films (Figure 4b). Thus, when analyzing TFT performance trends, while the carrier mobility increases because of trap prefilling, without the presence of a considerably less dense second or third layers to control the carrier density, V_T exhibits a negative shift, as expected for bulk-doped films.[13] When PEI content exceeds a critical point, and the mobility of PEI-doped IZO and IGZO devices begins to fall, V_T will also begin to shift positively, as additional PEI disrupts film continuity and introduces more traps. Regarding IGO:*x* wt% PEI TFTs, although a layering is observable in the channel layer (Figure 4d), a peak in mobility at 1.0 wt% PEI and a continuous negative V_T shift are observed. This reflects the strong Ga−O chemical bonding, suppressing intrinsic carrier formation and O vacancies. Moreover, the layered structure in IGO:*x* wt% PEI films is not as distinct as in In_2O_3:*x* wt% PEI films. Thus, the PEI electron doping capacity suppresses the multilayer functionality and leads to negatively shifted V_Ts. To further prove that the unique V_T trend for In_2O_3 is the combined effect of both film microstructure and intrinsic carrier concentration of the initial matrix, In_2O_3 TFTs processed at lower temperatures (200 and 225 °C) were fabricated. Note, reducing the annealing temperature of solution-processed In_2O_3 reduces the carrier concentration. The transfer curves of these devices along with the corresponding mobility and threshold voltage trends are shown Figures S28−S30. The results are fully consistent with the expectation, with overall lower mobilities, absence of a mobility peak for the device processed at the lowest temperature, and V_T first shifting negative for a low PEI content and then positive for higher PEI contents, of data which mimic the situation of IGO-based TFTs.

Based on the above results, it is physically reasonable that the inferior surface morphology and M-O-M lattice evolution in IZO (In:Zn = 70:30) and IGZO (In:Ga:Zn = 72.5:7.5.20) with increased PEI content (≥1.0 wt%), underlies the mobility peak obtained at 0.5 wt% PEI, while in In_2O_3:*x* wt% PEI films and IGO:*x* wt% PEI films, the mobility peaks at ∼1.0 wt% PEI, as shown in Figure 1d. Therefore, it is expected that the optimal PEI concentration yielding μ_{peak}, may shift to even greater values (∼1.0 wt%) with decreased Zn content in IZO, since lower Zn content will reduce surface roughness and increase M-O-M lattice content on PEI incorporation. On the other hand, the optimal PEI content for IGO should not be affected by the Ga composition since the Ga in the IGO:*x* wt% PEI films affects neither the film morphology nor the M-O-M lattice condensation. Furthermore, note that while the starting matrices for IZO(70:30), IGO(70:30), and IGZO(72.5:7.5:20) are all amorphous (Figure S20), In_2O_3 is polycrystalline. In the following section, we report experiments designed address these questions and whether it is possible to distinguish/understand the effects of metal variation and composition vs the structural differences the starting MO matrices.

IZO Films and Transistors. To probe the influence on transport of the metal composition and microstructure of the starting MO matrix, IZO(*a*:*b*):*x* wt% PEI films (*a*:*b* = %In:%Zn atomic ratios) with lower Zn contents and the corresponding TFTs were investigated. IZO(96:4):*x* wt% PEI compositions were first investigated considering that IZO films (In:Zn = 96:4) without PEI annealed at T_{ann} = 300 °C are polycrystalline (*vide infra*). This experiment permits a systematic comparison between In_2O_3 and IZO films/devices, considering that both starting matrices are polycrystalline. Similarly to In_2O_3: *x* wt% PEI (T_{ann} = 250 °C), the GIXRD data of IZO(96:4):*x* wt% PEI films in Figure S31 reveal a microstructural evolution from crystalline to amorphous as the PEI content increases. Thus, the crystalline content of In_2O_3: *x* wt% PEI and IZO(96:4):*x* wt% PEI films decreases from 70%

DOI: 10.1021/jacs.8b01252
J. Am. Chem. Soc. 2018, 140, 5457−5473

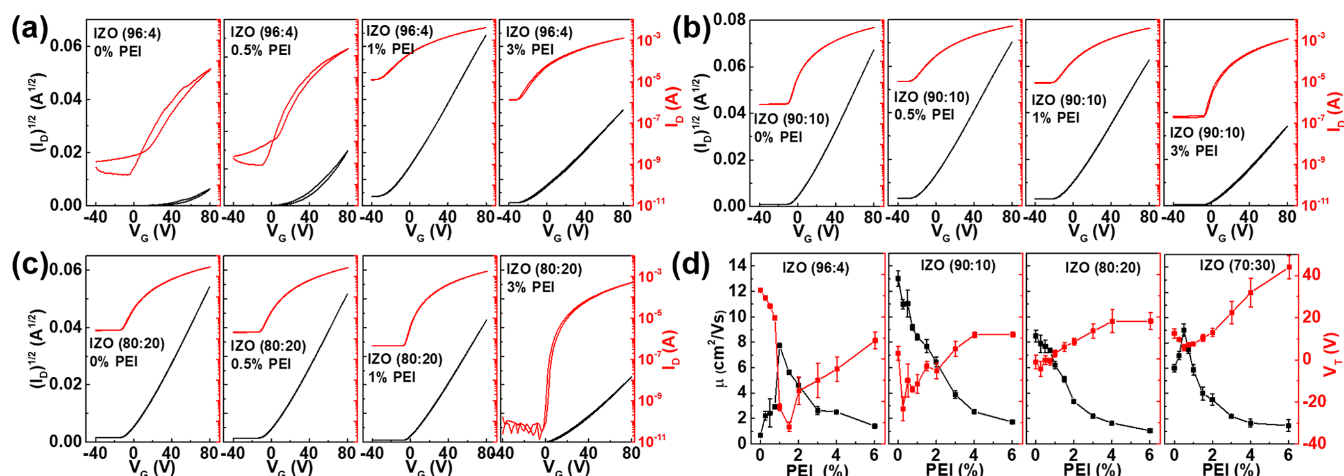

Figure 6. Representative TFT transfer characteristics for the indicated films: (a) IZO(96:4):x wt% PEI, (b) IZO(90:10):x wt% PEI, and (c) IZO(80:20):x wt% PEI TFTs. V_D = +80 V. (d) Electron mobility and threshold voltage for TFTs based on IZO(a:b):x wt% PEI with different In:Zn molar ratios as a function of the PEI concentration. T_{ann} = 300 °C.

and 81% (0.0 wt% PEI) to 50% and 46% (0.5 wt% PEI), 19% and 8% (1.0 wt% PEI), 9% and 7% (1.5 wt% PEI), 7% and 2% (3.0 wt% PEI), respectively. AFM images of IZO(96:4): x wt% PEI films (Figure S32) indicate relatively smooth film surfaces (σ_{RMS} = 0.19−0.35 nm) similar to those of In_2O_3 films, rather than the rough surfaces of IZO(70:30): x wt% PEI compositions. Finally, XPS O 1s analysis (Figures S33 and S34) indicates that the M-O-M lattice of IZO(96:4) films with increasing the PEI content, only slightly decreases from 79.2% (0.0 wt% PEI) to 73.7% (3.0 wt% PEI), versus the sharp decrease [from 79.6% (0.0 wt% PEI) to 64.4% (3.0 wt% PEI)] observed in IZO(70:30).

Next, the performance of IZO(96:4) TFTs was investigated and representative I−V characteristics are shown in Figures 6a and S35. The results are surprising and differ from expectation. Compared to the IZO(70:30) devices, the TFTs based on IZO(96:4) without any PEI have poor transfer characteristics, including a low I_{ON} of 4.03 × 10^{-5} A ($I_{OFF} \approx 10^{-10}$ A) along with appreciable I−V hysteresis. As the PEI content increases to 1.0 wt% the TFT performance gradually increases with both higher I_{OFF} (∼10^{-5} A) and I_{ON} (4.13 × 10^{-3} A), then falls as the PEI content rises to >1.0 wt%. Note that PEI doping always reduces I−V hysteresis independent of the doping level. By analyzing the transfer curves, it is found that PEI-doped IZO(96:4) transistors also exhibit a peak mobility (7.74 cm^2/(V·s)) at a ∼ 1.0 wt% PEI doping concentration (Figure 6d). However, the mobility of the undoped polycrystalline IZO(96:4) is very low (<1.0 cm^2/(V·s)), consistent with previous reports on polycrystalline IZO TFTs.[69] Regarding V_T, a considerable negative shift from +32.5 V (0.0 wt% PEI) to −32.0 V (1.5 wt% PEI) is obtained, followed by a positively shifted V_T in the PEI doping range 2.0−6.0 wt%. This result agrees with literature data arguing that the performance of polycrystalline IZO-based (grown by sputtering or PLD)[69,70] and In_2O_3-based (grown by PLD)[71] TFTs is inferior to that of the corresponding amorphous MO TFTs, due principally to suppressed electron scattering at the grain boundaries. Moreover, the extraordinary low performance of IZO(96:4) TFTs compared to that of polycrystalline In_2O_3 TFTs, is possibly due to phase separation of In_2O_3 and ZnO crystals, which significantly increase the grain boundary energy barrier.[69] Thus, PEI doping yields amorphous IZO films with dramatically enhanced carrier mobilities, likely due to a combination of PEI electron doping (as in the case of amorphous IZO(70:30)) and suppression of grain boundary scattering effects.

Next, transistors based on IZO(a:b):x wt% PEI films with In:Zn = 90:10 and 80:20 ratios with all compositions having amorphous matrices, were fabricated and characterized. As shown in Figures 6, S36, and S37, when the PEI content increases from 0.0 to 0.25 wt%, the I_{ON} for IZO(90:10) and IZO(80:20) increases minimally from 4.32 × 10^{-3} A and 2.84 × 10^{-3} A (0.0 wt% PEI), to 6.45 × 10^{-3} A and 3.75 × 10^{-3} A (0.25 wt% PEI), respectively, indicating that PEI is effective in donating electrons in these IZO compositions. Higher PEI contents monotonously decrease I_{ON} to 3.92 × 10^{-3} A and 1.81 × 10^{-3}A (1.0 wt% PEI), 1.17 × 10^{-3} A and 5.19 × 10^{-4} A (3.0 wt% PEI), and 4.25 × 10^{-4} A and 1.78 × 10^{-4} A (6.0 wt% PEI), respectively. However, the mobilities decrease monotonically with increasing the PEI content for both the IZO(90:10) and IZO(80:20) compositions, from 13.02 cm^2/(V·s) and 8.49 cm^2/(V·s) (0.0 wt% PEI) to 10.99 cm^2/(V·s) and 7.93 cm^2/(V·s) (0.25 wt% PEI) to 8.41 cm^2/(V·s) and 6.20 cm^2/(V·s) (1.0 wt% PEI), and all the way to 1.71 cm^2/(V·s) and 1.03 cm^2/(V·s) (6.0 wt% PEI), respectively (Figure 6d). In contrast, the V_Ts of both compositions exhibit an initial negative shift going from the undoped to the 0.5 wt% PEI samples, and then monotonically shift positive as the PEI content increases. This behavior indicates that PEI can transfer electrons into all these MO compositions; however, their mobility invariably decreases, even for very low PEI loadings, possibly because of the absence of a crystalline → amorphous transition combined with a high carrier density causing lattice scattering/ionized impurity scattering. The latter is a well-known phenomenon in amorphous IZO or In_2O_3 films with high carrier concentrations.[72,73]

Based on the TFT performance of all PEI-doped IZO(a:b):x wt% PEI films [a:b = 96:4, 90:10, 80:20, 70:30], it can be concluded that PEI effects on electron mobility are highly sensitive to the initial IZO matrix morphology (crystalline vs amorphous) and to the In:Zn molar ratio. Thus, for starting undoped crystalline MO matrices, such as IZO(96:4), significant grain boundaries lead to inferior TFT performance. Here, PEI addition results in amorphization, electron doping,

DOI: 10.1021/jacs.8b01252
J. Am. Chem. Soc. 2018, 140, 5457−5473

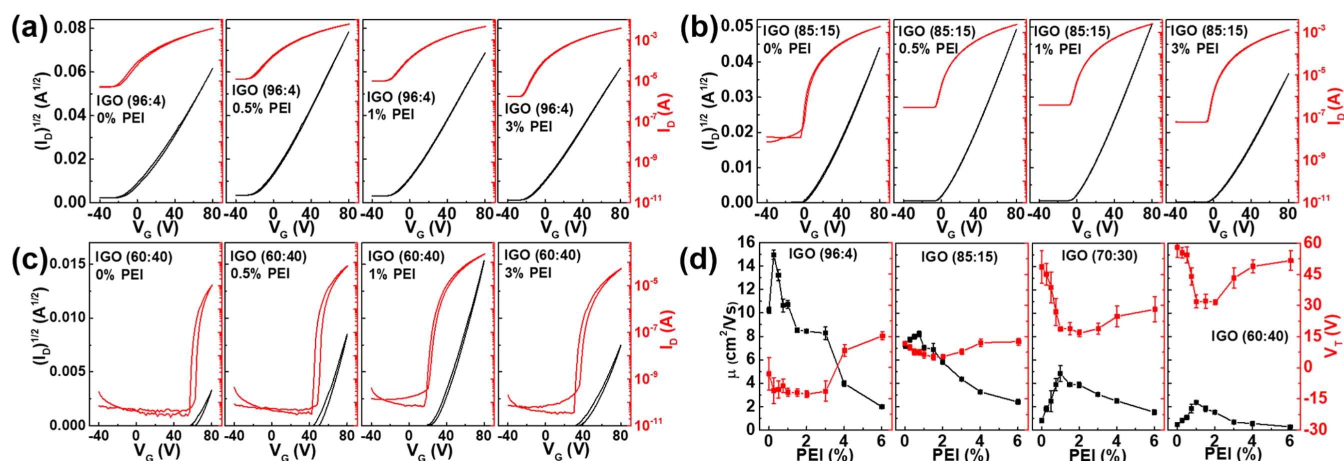

Figure 7. Representative TFT transfer characteristics for the indicated films: (a) IGO(96:4):x wt% PEI, (b) IGO(85:15):x wt% PEI, and (c) IGO(60:40):x wt% PEI TFTs. V_D = +80 V. (d) Electron mobility and threshold voltage for TFTs based on IGO(a:c):x wt% PEI with different In:Ga molar ratios as a function of the PEI concentration. T_{ann} = 300 °C.

and an enhanced mobility for PEI contents ≤1.0 wt%. For the IZO(90:10) and IZO(80:20) compositions, since the carrier density of these amorphous films is already relatively high, PEI addition will contribute more electrons, which further increases the carrier concentration, limiting the electron transport in these films by lattice scattering or ionized impurity scattering. This result is in agreement with the large I_{ON} and I_{OFF} currents (low I_{ON}:I_{OFF}), mobility reduction, and, for very low PEI loading, a negative V_T shift. Thus, no mobility peak is observed. On the other hand, for undoped amorphous MO matrices with a high Zn content, as in the case of the IZO(70:30), since Zn suppresses the intrinsic carrier density in solution processed IZO, the PEI doping effect results in a peak mobility for an optimal PEI content as well as a V_T first shifting negative due to trap prefilling and then positive, with a corresponding mobility decrease, as the result of excessive polymer loading.

IGO Films and Transistors. To understand the trends observed above and corroborate the interplay between film elemental composition and PEI doping, we investigated in more detail IGO(a:c) metal compositions (a:c = %In:%Ga atomic ratios) considering the far stronger oxygen getter affinity of Ga vs Zn[55] and optimal IGO vs IZO film morphologies (*vide supra*, Figure 2). Thus, IGO(a:c):x wt% PEI-doped film TFTs with differing In:Ga ratios [96:4 (polycrystalline matrix), 85:15, 70:30, and 60:40 (exclusively amorphous matrices)] were fabricated. All films were annealed at 300 °C. Compared to the IZO:x wt%PEI films, all of these IGO films are very smooth (σ_{RMS} ≈ 0.3 nm) and there is no significant decrease in the M-O-M lattice content, which remains in the 75–80% range, as assessed by AFM and XPS analysis, respectively (Figures 2 and 3). As shown in Figures 7, S3, and S38–S40, small amounts of PEI always increase IGO TFT I_{ON} and reduce hysteresis, indicating that PEI addition efficiently donates electrons to all IGO films. Thus, I_{ON} increases from 3.79 × 10^{-3} A (In:Ga = 96:4, 0.0 wt% PEI), 1.82 × 10^{-3} A (In:Ga = 85:15, 0.0 wt% PEI), 2.86 × 10^{-5} A (In:Ga = 70:30, 0.0 wt% PEI), and 1.11 × 10^{-5} A (In:Ga = 60:40, 0.0 wt% PEI) and will peak, for different PEI contents, to a maximum I_{ON} value of 6.44 × 10^{-3} A (In:Ga = 96:4, 0.25 wt% PEI), 2.57 × 10^{-3} A (In:Ga = 85:15, 0.75 wt% PEI), 1.16 × 10^{-3} A (In:Ga = 70:30, 1.0 wt% PEI), and 2.35 × 10^{-4} A (In:Ga = 60:40, 1.0 wt% PEI), and then decrease to 4.77 × 10^{-4} A (IGO(96:4)), 6.22 × 10^{-4} A (IGO(85:15)), 2.01 × 10^{-4} A (IGO(70:30)), and 1.53 × 10^{-5} A (IGO(60:40)) for the 6.0 wt% PEI containing films. The variation of I_{ON} for the PEI-free compositions is expected considering the oxygen getter effects of Ga—increasing the Ga content in IGO films will reduce the carrier concentration.

Figure 7d shows the mobility and V_T dependence for TFTs having all IGO compositions as a function of the PEI content. As expected, for a given PEI content, the carrier mobility decreases and the V_T shifts to more positive values as the Ga content increases. For instance, the mobility of IGO(a:c) TFTs without PEI doping decreases from 10.23 $cm^2/(V{\cdot}s)$ for IGO(96:4) to 7.30 $cm^2/(V{\cdot}s)$ for IGO(85:15) to 0.82 $cm^2/(V{\cdot}s)$ for IGO(70:30) to 0.46 $cm^2/(V{\cdot}s)$ for IGO(60:40), while V_T shifts from −3.0 V (IGO(96:4)) to +11.8 V (IGO(85:15)) to +48.6 V (IGO(70:30)) to +58.1 V (IGO(60:40)). In contrast to IZO:x wt%PEI TFTs, and independent of the In/Ga molar ratio and MO starting matrix microstructure, PEI addition invariably yields a mobility peak. For IGO(96:4) films, a peak of 14.97 $cm^2/(V{\cdot}s)$ is obtained for a PEI content of 0.25 wt%. Interestingly, increasing the film Ga content gradually shifts the optimal PEI concentration to a greater value, such as 0.75 wt% PEI with a μ_{peak} = 8.22 $cm^2/(V{\cdot}s)$ for IGO(85:15) and 1.0 wt% PEI with a μ_{peak} = 4.85 $cm^2/(V{\cdot}s)$ and 2.37 $cm^2/(V{\cdot}s)$ for IGO(70:30) and IGO(60:40), respectively. With respect to V_T, the lowest V_T values [~ −12 V for IGO(96:4), ~ +5 V for IGO(85:15), ~ +17 V for IGO(70:30), ~ +32 V for IGO(60:40)] are found at ~1.0–2.0 wt% PEI concentrations in all four types of IGO transistors.

From the above results, we conclude that the optimal PEI content to yield peak mobilities depends not only on the oxide composition but, equally important, on the metal molar ratio. Moreover, the optimal PEI content at which μ maximizes, for a given IZO or IGO composition, shifts to larger values as the Zn or Ga content increases (Figures 6 and 7). It is known that doping heavy metal oxides, such as In_2O_3, with light metals such as Ga or Zn significantly affects the oxide electronic structure, e.g., Ga doping widens the band gap, raising the CBM and lowering the VBM, and shifting the WF upward or downward depending on the Ga content.[74−76] Thus, an interesting question that arises is whether a correlation exists between establishing a mobility peak, the optimal PEI content at which this occurs, the PEI electron doping capacity, and the electronic structure of the MO film.

DOI: 10.1021/jacs.8b01252
J. Am. Chem. Soc. 2018, 140, 5457−5473

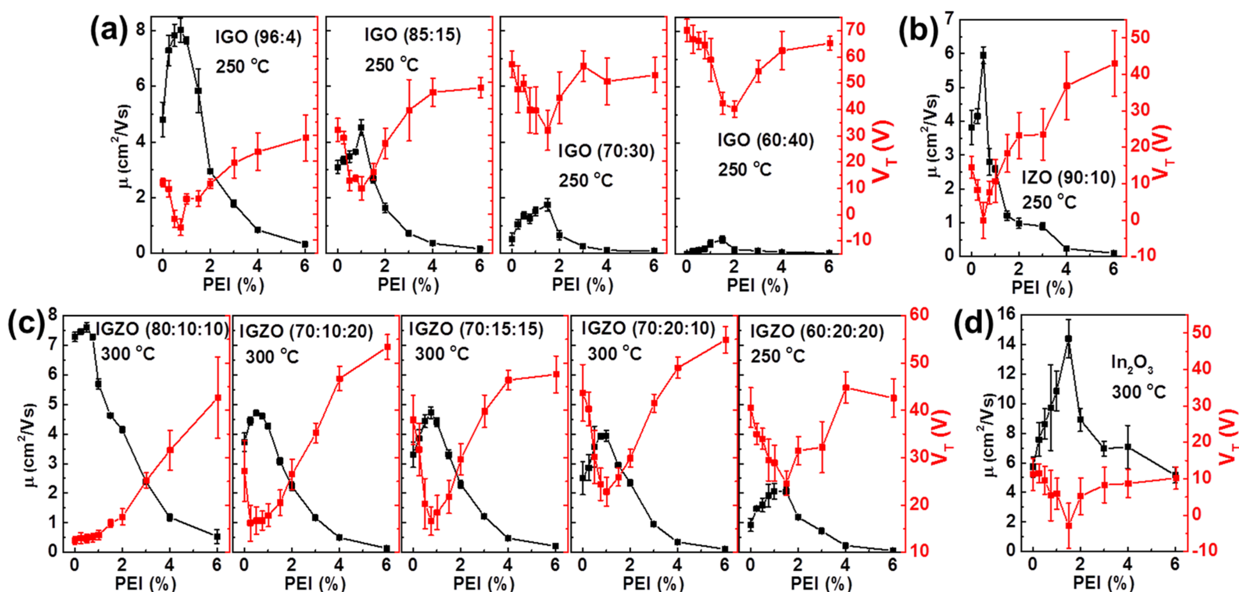

Figure 8. TFT mobility and threshold voltage for (a) IGO:*x* wt% PEI (T_{ann} = 250 °C), (b) IZO(90:10):*x* wt% PEI (T_{ann} = 250 °C), (c) IGZO:*x* wt% PEI (T_{ann} = 300 °C), and (d) In_2O_3:*x* wt% PEI (T_{ann} = 300 °C) based TFTs as a function of the polymer concentration.

Table 2. Mobility (μ) and Work Function (WF) Data for Neat Metal Oxide Matrices and Peak Mobility (μ_{peak}) for MO:*x* wt% PEI Films at the Indicated PEI Content

MO	atomic molar ratio	T_{ann} (°C)[a]	no PEI μ ($cm^2/(V{\cdot}s)$)	no PEI WF (eV)	μ_{peak} ($cm^2/(V{\cdot}s)$) [wt% PEI]
In_2O_3	NA	250[p]	4.18	4.06	8.37 [1 wt%]
		300[p]	5.73	3.96	14.40 [1.5 wt%]
IZO(*a*:*b*)	96:4	250[a]		3.96	
		300[p]	0.68	3.86	7.74 [1 wt%]
	90:10	250[a]	3.82	4.18	5.95 [0.5 wt%]
		300[a]	13.02	4.02	13.02 [no peak]
	80:20	250[a]		4.24	
		300[a]	8.49	4.08	8.49 [no peak]
	70:30	250[a]		4.21	
		300[a]	6.01	4.13	9.03 [0.5 wt%]
IGO(*a*:*c*)	96:4	250[a]	4.81	4.11	8.02 [0.75 wt%]
		300[p]	10.23	3.95	14.97 [0.25 wt%]
	85:15	250[a]	3.10	4.18	4.52 [1 wt%]
		300[a]	7.30	4.09	8.22 [0.75 wt%]
	70:30	250[a]	0.51	4.30	1.75 [1.5 wt%]
		300[a]	0.82	4.22	4.85 [1 wt%]
	60:40	250[a]	0.01	4.28	0.53 [1.5 wt%]
		300[a]	0.46	4.20	2.37 [1 wt%]
IGZO(*a*:*c*:*b*)	80:10:10	300[a]	7.28	4.10	7.61 [0.5 wt%]
	70:10:20	300[a]	3.72	4.19	4.71 [0.5 wt%]
	70:15:15	300[a]	3.30	4.20	4.72 [0.75 wt%]
	70:20:10	300[a]	2.51	4.21	3.92−3.94 [0.75−1 wt%]
	60:20:20	300[a]	0.93	4.20	2.06−2.07 [1−1.5 wt%]

[a]p = polycrystalline; a = amorphous.

Charge Transport vs MO:PEI Film Electronic Structure. To address the questions posed above, two additional sets of experiments were carried out: (1) Characterize TFTs based on new MO compositions with IO/IZO/IGO matrices processed at temperatures (T_{ann}) not investigated previously and IGZO matrices with different metal molar ratios (Figures S41−S51). (2) Assess the WFs of MO films by UPS (Figures S52 and S53). Note, the WF here is calculated by using the equation WF = $h\nu - E_{cutoff}$, where $h\nu$ = 21.21 eV and E_{cutoff} is the cross point of the linear exploration of high binding energy cutoffs with the background line in the UPS spectra.

DOI: 10.1021/jacs.8b01252
J. Am. Chem. Soc. 2018, 140, 5457−5473

Figure 8 presents the mobility/V_T-PEI content plots for the additional MO TFTs investigated here. These include IGO-(*a*:*c*) films processed at 250 °C (Figure 8a), IZO(90:10) (T_{ann} = 250 °C, Figure 8b), IGZO(*a*:*c*:*b*) films processed at 300 °C (Figure 8c), and In_2O_3 films (T_{ann} = 300 °C, Figure 8d). Detailed comments on the characteristics of these devices can be found in the SI, and Table 2 summarizes all of the MO matrices specifying which ones are polycrystalline/amorphous and the corresponding TFT mobilities for all the PEI-undoped devices. Briefly, for the IGO(*a*:*c*)-based transistors, when moving from a T_{ann} of 300 °C (*vide supra*) to 250 °C, the optimal PEI concentration for the peak mobility shifts to larger values, thus, from 0.25 wt% to 0.75 wt% PEI for IGO(96:4), from 0.75 wt% to 1 wt% PEI for IGO(85:15), and from 1 wt% to 1.5 wt% PEI for both IGO(70:30) and IGO(60:40). Unlike the IZO(90:10) films annealed at 300 °C, which do not exhibit a mobility peak upon PEI doping, IZO(90:10) TFTs annealed at 250 °C exhibit an obvious peak of 5.9 5 $cm^2/(V \cdot s)$ for a 0.5 wt% PEI content. All of the IGZO(*a*:*c*:*b*) compositions exhibit a mobility peak on PEI doping, with the optimal PEI content increasing as the Ga content (*c*) increases from 10% to 20%. Thus, for PEI-free IGZO(*a*:*c*:*b*) matrices the TFT mobility falls from 7.28 $cm^2/(V \cdot s)$ for IGZO(80:10:10), to 3.72 $cm^2/(V \cdot s)$ for IGZO(70:10:20), 3.30 $cm^2/(V \cdot s)$ for IGZO(70:15:15), 2.51 $cm^2/(V \cdot s)$ for IGZO(70:20:10), and 0.93 $cm^2/(V \cdot s)$ for IGZO(60:20:20), to a μ_{peak} = 7.61 $cm^2/(V \cdot s)$ for IGZO(80:10:10):0.5 wt% PEI, 4.71 $cm^2/(V \cdot s)$ for IGZO(70:10:20):0.5 wt% PEI, 4.72 $cm^2/(V \cdot s)$ for IGZO(70:15:15):0.75 wt% PEI, 3.92–3.94 $cm^2/(V \cdot s)$ for IGZO(70:20:10):0.75–1 wt% PEI, and 2.06–2.07 $cm^2/(V \cdot s)$ for IGZO(60:20:20):1–1.5 wt% PEI devices. For an excessive PEI content of 6.0 wt%, the mobility falls to 0.54 $cm^2/(V \cdot s)$ for IGZO(80:10:10), 0.14 $cm^2/(V \cdot s)$ for IGZO(70:10:20), 0.21 $cm^2/(V \cdot s)$ for IGZO(70:15:15), 0.11 $cm^2/(V \cdot s)$ for IGZO(70:20:10), and 5.8 × 10^{-2} $cm^2/(V \cdot s)$ for IGZO(60:20:20). Finally, the In_2O_3: *x* wt%PEI devices annealed at 300 °C also exhibit a mobility peak as do the In_2O_3 blends annealed at a lower temperature (T_{ann} = 250 °C, *vide supra*). The mobility peak of 14.40 $cm^2/(V \cdot s)$, vs 5.73 $cm^2/(V \cdot s)$ for undoped In_2O_3-based transistors, is established for a 1.5 wt% PEI content, which is larger than that for the 250 °C annealed devices (1.0 wt% PEI, μ_{peak} = 8.37 $cm^2/(V \cdot s)$).

Figure 9 reports the peak mobilities for all compositions investigated in this study, along with the mobility of the corresponding undoped MO matrices, which demonstrate that PEI doping can enhance the MO TFT electron mobility for solution-processed MO films to as high as ~15 $cm^2/(V \cdot s)$. From this composition-mobility plot, it is obvious that higher annealing temperatures will effectively enhance the mobility, as shown for the neat In_2O_3, IGO and IZO as well as for all of the MO:*x* wt%PEI devices. On the other hand, the mobilities of the oxide matrices decrease as the Ga and/or Zn content increases. Similar trends are also found for the peak mobility of the MO:*x* wt%PEI TFTs with optimal PEI contents. Note that the In_2O_3 and IZO(96:4) devices fall outside these trends because the highly polycrystalline nature of these film s introduces grain boundary scattering, resulting in depressed mobilities versus those incorporating Zn/Ga or additional Zn, respectively. Furthermore, the PEI capacity to increase mobility is more pronounced when the neat metal oxide film is polycrystalline and for compositions rich in Ga and/or Zn. Thus, the mobility of IGO(85:15) only increases from 3.10 $cm^2/(V \cdot s)$ (250 °C) and 7.30 $cm^2/(V \cdot s)$ (300 °C) to 4.52 $cm^2/(V \cdot s)$(250 °C) and

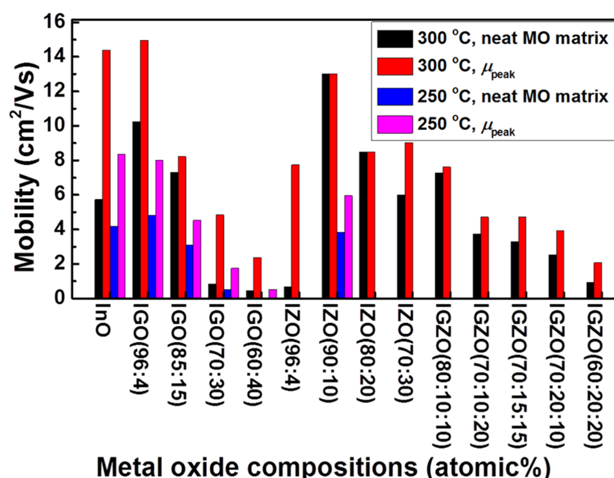

Figure 9. Mobilities of neat metal oxide based transistors (black bars for T_{ann} = 300 °C; blue bars for T_{ann} = 250 °C) and peak mobility of the corresponding PEI-doped metal oxide based transistors with the optimal PEI content (red bars for T_{ann} = 300 °C and magenta bars for T_{ann} = 250 °C). Note, for IZO(90:10) and IZO(80:20) (T_{ann} = 300 °C) the black/red bars are identical since these is no mobility peak.

8.22 $cm^2/(V \cdot s)$ (300 °C), respectively, which is a variation of about +46% and +13%, respectively. The mobility of IGZO(80:10:10, 300 °C) only increases 5% (from 7.28 $cm^2/(V \cdot s)$ to 7.61 $cm^2/(V \cdot s)$). However, for the IGO(60:40) devices the mobility increases from 0.01 $cm^2/(V \cdot s)$ (250 °C) and 0.46 $cm^2/(V \cdot s)$ (300 °C) to 0.53 $cm^2/(V \cdot s)$ (250 °C) and 2.37 $cm^2/(V \cdot s)$ (300 °C). These data correspond to increases as high as ~+5000% (250 °C) and ~+400% (300 °C). Significant mobility increases of 120% (from 0.93 $cm^2/(V \cdot s)$ to 2.06 $cm^2/(V \cdot s)$, IGZO(60:20:20), 300 °C), 151%(from 5.73 $cm^2/(V \cdot s)$ to 14.4 $cm^2/(V \cdot s)$, In_2O_3, 300 °C), 100%(from 4.18 $cm^2/(V \cdot s)$ to 8.37 $cm^2/(V \cdot s)$, In_2O_3, 250 °C), and 1000%(from 0.68 $cm^2/(V \cdot s)$ to 7.74 $cm^2/(V \cdot s)$, IZO(96:4), 300 °C) are also obtained. The above results indicate that the tendency of PEI to enhance charge transport is significant, and enhanced by amorphization and the prefilling of shallow traps.

The WF values of relevant MO matrices (no PEI addition) are also summarized in Table 2. These data indicate that, for a given processing temperature, the WF of IZO, IGO, and IGZO matrices with different metal atomic ratios shifts to statistically higher values as the Zn and/or Ga content increases. Thus, for IZO(*a*:*b*) and IGO(*a*:*c*) films processed at 300 °C, the WF increases from 3.86 to 4.13 eV and 3.95 to 4.22 eV, respectively, when b and c increase from 4% to 30% or 40%. Furthermore, by analyzing IZO(*a*:*b*) and IGO(*a*:*c*) matrices processed at the same temperature and with the same Zn and Ga content (*b* = *c*), it is clear that Ga is more effective than Zn in increasing the WF. This result is corroborated further by the greater WF of IGZO(80:10:10) (4.10 eV) and IGZO(70:*c*:*b*) (4.19–4.21 eV) vs IZO(80:20) (4.08 eV) and IZO(70:30) (4.13 eV) compositions having the same Zn+Ga content vs that of In. Finally, for MOs with identical composition, those annealed at 250 °C invariably have a higher WF by ~0.06–0.16 eV than those annealed at 300 °C.

When analyzing the WF data for the pristine amorphous matrices and the blend compositions where the mobility peaks, the general trend is that optimal PEI contents yielding μ_{peak} increase as the MO matrix WF increases (see Table 2 and Figure 9). For example, for the 300 °C annealed IGO(*a*:*c*)

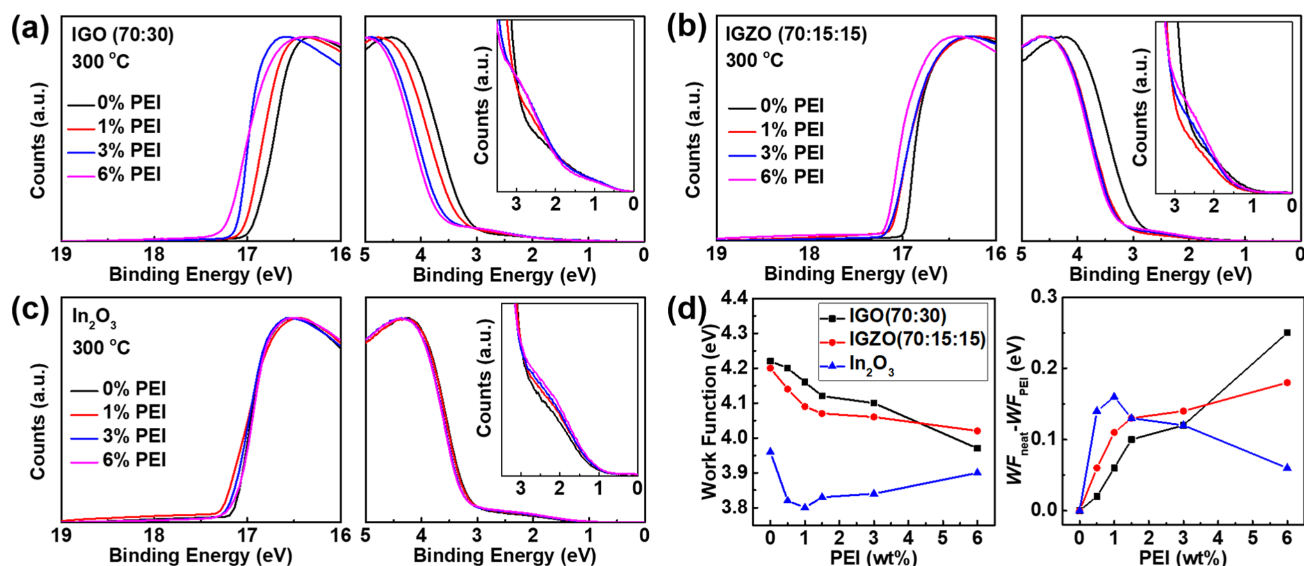

Figure 10. Representative cutoff and valence band regions of the UPS spectra of (a) IGO(70:30, T_{ann} = 300 °C), (b) IGZO(70:15:15, T_{ann} = 300 °C), and (c) In_2O_3 (T_{ann} = 300 °C) films as a function of PEI doping concentration. E_F level is set at 0.0 eV. The insets focus on sub-gap states. (d) WF values (left) and variations versus the pristine matrix set as zero (right) as a function of PEI content for the indicated metal oxides:*x* wt% PEI.

series, the optimal PEI content/WF increases from 0.25 wt %/3.95 eV for IGO(96:4) to 0.75 wt%/4.09 eV for IGO(85:15), to 1.0 wt%/4.20−4.22 eV for IGO(70:30) and IGO(60:40). Similar trends are observed for IGO(*a*:*c*) processed at 250 °C, where the optimal PEI content increases from 0.75 wt% to 1.5 wt% as the WF increases from 4.11 eV to 4.28−4.30 eV as well as for amorphous IZO(*a*:*b*) TFTs processed at 300 °C, where compositions without a mobility peak [IZO(90:10) and IZO(80:20)] with WF = 4.02 and 4.08 eV, respectively, exhibit a mobility peak at a PEI content = 0.5 wt% as in IZO(70:30) having a WF of 4.13 eV. For IGZO, the optimal PEI content also increases along with the WF, rising from 0.5 wt%/4.10 eV for IGZO(80:10:10) to 0.75 wt%/4.19 eV for IGZO(70:15:15), to 1.5 wt%/4.20 eV for IGZO(60:20:20).

Furthermore, for the same composition, since a lower processing temperature increases the WF, the mobility peak consistently occurs at higher PEI contents when the film annealing temperature is lowered. Thus, it appears that the PEI loadings required for optimum charge transport correlate with the neat metal oxide matrix WFs.

To investigate the above trends further, UPS measurements were carried out for selected PEI-doped IGO, IGZO and In_2O_3 samples (Figure S52 and Table S3). As shown in Figures 10a, the WF of the IGO(70:30, 300 °C) film shifts monotonically from 4.22 eV (0.0 wt% PEI) to 4.16 eV (1.0 wt% PEI) to 4.10 eV (3 wt% PEI) to 3.97 eV (6 wt% PEI). This result suggests that electron transfer from PEI to the MO matrix continues as the PEI content increases, furthermore, at 6.0 wt% PEI although slowing down has not reached equilibrium. Note that experiments were carried out with greater PEI loadings of 12 and 24 wt%; however, because of the very poor film morphologies, reliable WF values could not be extracted and are not shown. For IGZO(70:15:15, 300 °C) films (Figure 10b), the WF shift is not as obvious as that in IGO(70:30, 300 °C); however, an overall decline in the WF from 4.20 eV (0.0 wt% PEI) to 4.09 eV (1.0 wt% PEI) to 4.06 eV (3 wt% PEI) to 4.02 eV (6 wt% PEI) is observed. Furthermore, the WF of In_2O_3 (300 °C) remains in a relatively narrow range (3.80−3.96 eV, Figure 10c) on PEI doping. However, note that the WFs of PEI-doped oxide films (3.80−3.90 eV in In_2O_3, 3.97−4.20 eV in IGO, and 4.02−4.14 eV in IGZO) are all lower than those of the corresponding neat matrices (3.96 eV in In_2O_3, 4.22 eV in IGO, and 4.20 eV in IGZO, Figure 10d). Although these variations in WF are significant, they are far less than those measured for 10 nm PEI-coated high-WF conductors such as ITO (4.30 → 2.94 eV) and Au (5.06 → 3.20 eV) (Figure S54 and Table S3), in accord with the literature.[77,78] Moreover, In_2O_3 (300 °C), IGO(70:30, 300 °C), and IGZO(70:15:15, 300 °C) films also show much larger WF shifts (In_2O_3, 3.96 → 2.80 eV; IGO, 4.22 → 2.82 eV; IGZO, 4.20 → 2.76 eV) when coated with 10 nm PEI. (Figure S54 and Table S3). These results indicate that PEI doping and electron transfer in preformed/bulk MO films is more effective than in blended PEI-MO systems as a result of microstructure disruption and creation of additional deep charge traps that the added electrons must fill. This result is further confirmed by carrying out the same experiment on prefabricated MO TFTs. As shown in Figure S55, coating IGO-, IGZO-, and In_2O_3-based transistors with a 10 nm thick PEI film increases the I_{ON} current dramatically [2.86×10^{-5} A → 1.54×10^{-3} A for IGO, 3.34×10^{-5} A → 3.22×10^{-3} A for IGZO, 1.99×10^{-3} A → $>10^{-2}$ A for In_2O_3; at V_G = 80 V], and V_{ON} shifts to large negative values, from +38 V in IGO, +24 V in IGZO, and −12 V in In_2O_3 to <-40 V in all three transistors, clearly demonstrating that mobile electrons are transferred from the PEI to the MO matrix.

That PEI chain incorporation indeed disrupts film microstructure and creates additional traps is supported by the UPS data. Close inspection of these spectra reveals the presence of valence band tails in all films, assignable to sub-gap states just above the VBM with binding energies of ~1.0−3.5 eV (Figure 10). Furthermore, the gap between the VBM and E_F enlarges with increased PEI doping, generating new sub-gap states for the 3.0 and 6.0 wt% PEI-doped films as shown in the insets of Figure 10. These deep sub-gap states in metal oxides are observed in low-quality IGZO films, depressing TFT mobility and positively shifting V_T.[18]

DOI: 10.1021/jacs.8b01252
J. Am. Chem. Soc. 2018, 140, 5457−5473

Based on the above UPS data, PEI doping of metal oxides effectively decreases the MO matrix WF, meaning that PEI transfers electrons to the oxide matrix, and the transfer process (WF shift) is atomic composition dependent. Thus, the higher WFs of IGO (4.22 eV, 70:30, 300 °C) and IGZO (4.20 eV, 70:15:15, 300 °C) versus In_2O_3 (3.96 eV, 300 °C), facilitate electron transfer from PEI to the metal oxide so that the WF shifts in IGO(70:30, 300 °C) and IGZO(70:15:15, 300 °C) are far greater than that in In_2O_3 (300 °C). However, note that excessive PEI doping creates charge scattering sites, forms less dense oxide films, and increases the deep sub-gap states (Figure 10, insets). Moreover, the WF decrease levels off [IGO(70:30, 300 °C) and IGZO(70:15:15, 300 °C)] or reverses [In_2O_3 (300 °C)] with excessive PEI (>3 wt%), as shown in Figure 10d. As a result, the ideal PEI content must optimize transport by balancing these phenomena.

Finally, to underscore the relationship between PEI electron doping ability, the creation of a mobility peak, achieving optimal PEI content, and the MO film electronic structure, the optimal PEI content yielding the maximum mobility is plotted as a function of the WF of the various neat metal oxide matrices in Figure 11. This highlights the polycrystalline matrices, Zn-rich amorphous matrices having substantial RMS roughness, and other amorphous compositions. Analysis of these data reveals three interesting points: (1) The optimal PEI content maximizing TFT mobility in these oxides is below 1.5 wt%. (2) A clear correlation between the MO matrix WF and optimal PEI content exists for all IGO(a:c) compositions, with that PEI content yielding the peak mobility gradually increasing from 0.0 wt% to 1.5 wt% as WF increases from ~3.95 eV to ~4.3 eV. Note, IGO(96:4) (T_{ann} = 300 °C) falls on this line because of the very low crystallinity (~20%) compared to polycrystalline In_2O_3/IZO matrices (70−85%), and undergoes complete amorphization at a very low PEI content (see Figure S56). The IZO and IGZO compositions approach the IGO correlation line as the Zn content falls. This result is in line with morphological and M-O-M lattice issues originating by combining PEI + Zn, which strongly enhances the film roughness and reduces the M-O-M lattice content. Thus, for these matrices the mobility peak occurs at lower PEI contents than expected. (3) All polycrystalline matrices lay above the linear correlation line, meaning that far more PEI is required to maximize the TFT mobility than required by the intrinsic MO electronic structure. This result agrees with a smooth transition upon PEI addition from a polycrystalline to an amorphous phase (see Figures S31 and S56), which reduces gain boundary scattering and suggests that for these low WF/polycrystalline compositions PEI is more effective in enhancing mobility via promoting amorphization, rather than by optimal trap prefilling with PEI-derived electrons.

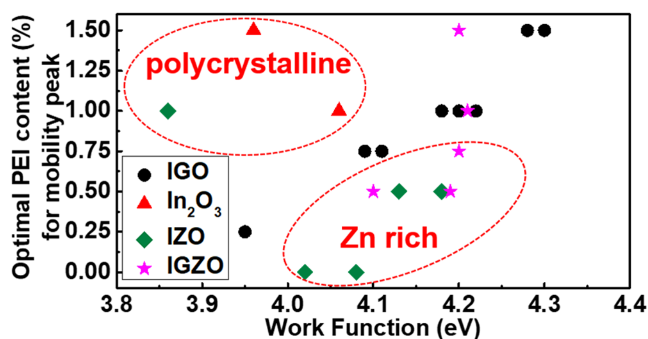

Figure 11. Optimal PEI content (wt%) yielding the maximum mobility with respect to the WF of different neat metal oxide matrices.

CONCLUSIONS

Incorporation of Zn and/or Ga into In_2O_3 thin films along with blending with electron-rich PEI provides important structural, electronic structure, and morphological information correlating the chemistry and composition of these metal oxide blends with the charge transport characteristics of the corresponding TFTs. First, PEI doping capability is universal in scope and can be expanded from binary In_2O_3 to ternary (e.g., In+Zn in IZO, In+Ga in IGO) and quaternary (e.g., In+Zn+Ga in IGZO) metal oxide matrices. Second, PEI ability to enhance TFT carrier mobility depends on the morphology (crystallinity) and elemental composition of the starting matrix. Third, the PEI content affording the best carrier mobility also depends on the aforementioned parameters as well as the WF of the starting matrix and the film morphology of the PEI-doped films. Thus, IGO(a:c) compositions exhibit a linear correlation between WF and optimal PEI content. Amorphous Zn-containing compositions approach linearity when the Zn content is very low, as the result of nonoptimal PEI+Zn film roughness. While highly crystalline neat metal oxide matrices always yield significantly increased mobility for PEI doping, this is a consequence of both electron doping and amorphization. The synergistic effects of added metal ions and PEI are therefore determined to be the principal origin of the observed TFT performance enhancement, demonstrating that engineering of both microstructure and energy levels is vital to controlling charge transport in hybrid amorphous oxide−polymer electronics.

ASSOCIATED CONTENT

Supporting Information

The Supporting Information is available free of charge on the ACS Publications website at DOI: 10.1021/jacs.8b01252.

Device fabrication process, transfer curves, AFM images, XPS data, XRD data, XRR data, TEM images, UPS data, and work function of metal oxide films, including Figures S1−S56 and Tables S1−S3 (PDF)

AUTHOR INFORMATION

Corresponding Authors

*a-facchetti@northwestern.edu
*t-marks@northwestern.edu
*bedzyk@northwestern.edu

ORCID

Wei Huang: 0000-0002-0973-8015
Peijun Guo: 0000-0001-5732-7061
Li Zeng: 0000-0001-6390-0370
Binghao Wang: 0000-0002-9631-6901
Junsheng Yu: 0000-0002-7484-8114
Michael J. Bedzyk: 0000-0002-1026-4558
Tobin J. Marks: 0000-0001-8771-0141

Notes

The authors declare no competing financial interest.

ACKNOWLEDGMENTS

We thank AFOSR (FA9550-15-1-0044), the Northwestern University MRSEC (NSF DMR-1720139), and Flexterra Corp. for support of this research. This work made use of the J. B.

Cohen X-ray Diffraction Facility, EPIC facility, Keck-II facility, and SPID facility of the NUANCE Center at Northwestern University, which received support from the MRSEC program (NSF DMR-1720139), the International Institute for Nanotechnology (IIN), the Keck Foundation, and the State of Illinois. A.F. thanks the Shenzhen Peacock Plan project (KQTD20140630110339343) for support. W.H. and B.W. thank the joint-Ph.D. program supported by the China Scholarship Council for fellowships.

REFERENCES

(1) Yu, X.; Smith, J.; Zhou, N.; Zeng, L.; Guo, P.; Xia, Y.; Alvarez, A.; Aghion, S.; Lin, H.; Yu, J.; Chang, R. P.; Bedzyk, M. J.; Ferragut, R.; Marks, T. J.; Facchetti, A. *Proc. Natl. Acad. Sci. U. S. A.* **2015**, *112*, 3217.
(2) Tate, J.; Ju, H. L.; Moon, J. C.; Zakutayev, A.; Richard, A. P.; Russell, J.; McIntyre, D. H. *Phys. Rev. B: Condens. Matter Mater. Phys.* **2009**, *80*, 165206.
(3) Petti, L.; Munzenrieder, N.; Vogt, C.; Faber, H.; Buthe, L.; Cantarella, G.; Bottacchi, F.; Anthopoulos, T. D.; Troster, G. *Appl. Phys. Rev.* **2016**, *3*, 021303.
(4) Fortunato, E.; Barquinha, P.; Martins, R. *Adv. Mater.* **2012**, *24*, 2945.
(5) Khim, D.; Lin, Y. H.; Nam, S.; Faber, H.; Tetzner, K.; Li, R.; Zhang, Q.; Li, J.; Zhang, X.; Anthopoulos, T. D. *Adv. Mater.* **2017**, *29*, 1605837.
(6) Kim, J.; Sekiya, T.; Miyokawa, N.; Watanabe, N.; Kimoto, K.; Ide, K.; Toda, Y.; Ueda, S.; Ohashi, N.; Hiramatsu, H.; Hosono, H.; Kamiya, T. *NPG Asia Mater.* **2017**, *9*, e359.
(7) Pecunia, V.; Banger, K.; Sirringhaus, H. *Adv. Electron. Mater.* **2015**, *1*, 1400024.
(8) Yu, X.; Marks, T. J.; Facchetti, A. *Nat. Mater.* **2016**, *15*, 383.
(9) Nomura, K.; Ohta, H.; Takagi, A.; Kamiya, T.; Hirano, M.; Hosono, H. *Nature* **2004**, *432*, 488.
(10) Kim, Y. H.; Heo, J. S.; Kim, T. H.; Park, S.; Yoon, M. H.; Kim, J.; Oh, M. S.; Yi, G. R.; Noh, Y. Y.; Park, S. K. *Nature* **2012**, *489*, 128.
(11) Kim, M. G.; Kanatzidis, M. G.; Facchetti, A.; Marks, T. J. *Nat. Mater.* **2011**, *10*, 382.
(12) Banger, K. K.; Yamashita, Y.; Mori, K.; Peterson, R. L.; Leedham, T.; Rickard, J.; Sirringhaus, H. *Nat. Mater.* **2011**, *10*, 45.
(13) Schiessl, S. P.; Faber, H.; Lin, Y. H.; Rossbauer, S.; Wang, Q.; Zhao, K.; Amassian, A.; Zaumseil, J.; Anthopoulos, T. D. *Adv. Mater.* **2016**, *28*, 3952.
(14) Hwang, S. W.; Park, G.; Cheng, H.; Song, J. K.; Kang, S. K.; Yin, L.; Kim, J. H.; Omenetto, F. G.; Huang, Y.; Lee, K. M.; Rogers, J. A. *Adv. Mater.* **2014**, *26*, 1992.
(15) Wang, B. H.; Yu, X. G.; Guo, P. J.; Huang, W.; Zeng, L.; Zhou, N. J.; Chi, L. F.; Bedzyk, M. J.; Chang, R. P. H.; Marks, T. J.; Facchetti, A. *Adv. Electron. Mater.* **2016**, *2*, 1500427.
(16) Wang, B.; Zeng, L.; Huang, W.; Melkonyan, F. S.; Sheets, W. C.; Chi, L.; Bedzyk, M. J.; Marks, T. J.; Facchetti, A. *J. Am. Chem. Soc.* **2016**, *138*, 7067.
(17) Cao, W. R.; Li, J.; Chen, H. Z.; Xue, J. G. *J. Photonics Energy* **2014**, *4*, 040990.
(18) Kamiya, T.; Nomura, K.; Hosono, H. *Sci. Technol. Adv. Mater.* **2010**, *11*, 044305.
(19) Chen, H.; Cao, Y.; Zhang, J.; Zhou, C. *Nat. Commun.* **2014**, *5*, 4097.
(20) Choi, C. H.; Lin, L. Y.; Cheng, C. C.; Chang, C. H. *ECS J. Solid State Sci. Technol.* **2015**, *4*, P3044.
(21) Liu, Y.; Guan, P. F.; Zhang, B.; Falk, M. L.; Katz, H. E. *Chem. Mater.* **2013**, *25*, 3788.
(22) Lin, Y. H.; Thomas, S. R.; Faber, H.; Li, R. P.; McLachlan, M. A.; Patsalas, P. A.; Anthopoulos, T. D. *Adv. Electron. Mater.* **2016**, *2*, 1600070.
(23) Lee, W. J.; Park, W. T.; Park, S.; Sung, S.; Noh, Y. Y.; Yoon, M. H. *Adv. Mater.* **2015**, *27*, 5043.
(24) Palneedi, H.; Park, J. H.; Maurya, D.; Peddigari, M.; Hwang, G. T.; Annapureddy, V.; Kim, J. W.; Choi, J. J.; Hahn, B. D.; Priya, S.; Lee, K. J.; Ryu, J. *Adv. Mater.* **2018**, *30*, 1705148.
(25) Fuchs, F.; Bechstedt, F. *Phys. Rev. B: Condens. Matter Mater. Phys.* **2008**, *77*, 155107.
(26) Noh, H. K.; Chang, K. J.; Ryu, B.; Lee, W. J. *Phys. Rev. B: Condens. Matter Mater. Phys.* **2011**, *84*, 115205.
(27) King, P. D. C.; Veal, T. D.; Fuchs, F.; Wang, C. Y.; Payne, D. J.; Bourlange, A.; Zhang, H.; Bell, G. R.; Cimalla, V.; Ambacher, O.; Egdell, R. G.; Bechstedt, F.; McConville, C. F. *Phys. Rev. B: Condens. Matter Mater. Phys.* **2009**, *79*, 205211.
(28) Liu, J.; Buchholz, D. B.; Hennek, J. W.; Chang, R. P.; Facchetti, A.; Marks, T. J. *J. Am. Chem. Soc.* **2010**, *132*, 11934.
(29) Khanal, R.; Buchholz, D. B.; Chang, R. P. H.; Medvedeva, J. E. *Phys. Rev. B: Condens. Matter Mater. Phys.* **2015**, *91*, 205203.
(30) Xu, J.; Liu, J.-B.; Liu, B.-X.; Li, S.-N.; Wei, S.-H.; Huang, B. *Adv. Electron. Mater.* **2018**, *4*, 1700553.
(31) Lee, S.; Jeon, S.; Chaji, R.; Nathan, A. *Proc. IEEE* **2015**, *103*, 644.
(32) Socratous, J.; Banger, K. K.; Vaynzof, Y.; Sadhanala, A.; Brown, A. D.; Sepe, A.; Steiner, U.; Sirringhaus, H. *Adv. Funct. Mater.* **2015**, *25*, 1873.
(33) Jin, S. H.; Kang, S. K.; Cho, I. T.; Han, S. Y.; Chung, H. U.; Lee, D. J.; Shin, J.; Baek, G. W.; Kim, T. I.; Lee, J. H.; Rogers, J. A. *ACS Appl. Mater. Interfaces* **2015**, *7*, 8268.
(34) Liu, G. X.; Liu, A.; Zhu, H. H.; Shin, B.; Fortunato, E.; Martins, R.; Wang, Y. Q.; Shan, F. K. *Adv. Funct. Mater.* **2015**, *25*, 2564.
(35) Nadaud, N.; Lequeux, N.; Nanot, M.; Jove, J.; Roisnel, T. *J. Solid State Chem.* **1998**, *135*, 140.
(36) Yu, X.; Zhou, N.; Smith, J.; Lin, H.; Stallings, K.; Yu, J.; Marks, T. J.; Facchetti, A. *ACS Appl. Mater. Interfaces* **2013**, *5*, 7983.
(37) Banger, K. K.; Peterson, R. L.; Mori, K.; Yamashita, Y.; Leedham, T.; Sirringhaus, H. *Chem. Mater.* **2014**, *26*, 1195.
(38) Park, W. T.; Son, I.; Park, H. W.; Chung, K. B.; Xu, Y.; Lee, T.; Noh, Y. Y. *ACS Appl. Mater. Interfaces* **2015**, *7*, 13289.
(39) Faber, H.; Lin, Y. H.; Thomas, S. R.; Zhao, K.; Pliatsikas, N.; McLachlan, M. A.; Amassian, A.; Patsalas, P. A.; Anthopoulos, T. D. *ACS Appl. Mater. Interfaces* **2015**, *7*, 782.
(40) Mativenga, M.; Geng, D.; Kim, B.; Jang, J. *ACS Appl. Mater. Interfaces* **2015**, *7*, 1578.
(41) Zhou, N.; Buchholz, D. B.; Zhu, G.; Yu, X.; Lin, H.; Facchetti, A.; Marks, T. J.; Chang, R. P. *Adv. Mater.* **2014**, *26*, 1098.
(42) Sallis, S.; Quackenbush, N. F.; Williams, D. S.; Senger, M.; Woicik, J. C.; White, B. E.; Piper, L. F. J. *Phys. Status Solidi A* **2015**, *212*, 1471.
(43) Hosono, H. *Thin Solid Films* **2007**, *515*, 6000.
(44) Kamiya, T.; Nomura, K.; Hosono, H. *Phys. Status Solidi A* **2009**, *206*, 860.
(45) Nomura, K.; Kamiya, T.; Hirano, M.; Hosono, H. *Appl. Phys. Lett.* **2009**, *95*, 013502.
(46) Yu, X.; Zeng, L.; Zhou, N.; Guo, P.; Shi, F.; Buchholz, D. B.; Ma, Q.; Yu, J.; Dravid, V. P.; Chang, R. P.; Bedzyk, M.; Marks, T. J.; Facchetti, A. *Adv. Mater.* **2015**, *27*, 2390.
(47) Huang, W.; Zeng, L.; Yu, X. G.; Guo, P. J.; Wang, B. H.; Ma, Q.; Chang, R. P. H.; Yu, J. S.; Bedzyk, M. J.; Marks, T. J.; Facchetti, A. *Adv. Funct. Mater.* **2016**, *26*, 6179.
(48) Liu, A.; Liu, G. X.; Zhu, H. H.; Shin, B. C.; Fortunato, E.; Martins, R.; Shan, F. K. *RSC Adv.* **2015**, *5*, 86606.
(49) Banger, K.; Warwick, C.; Lang, J.; Broch, K.; Halpert, J. E.; Socratous, J.; Brown, A.; Leedham, T.; Sirringhaus, H. *Chem. Sci.* **2016**, *7*, 6337.
(50) Kim, T.; Nam, Y.; Hur, J. H.; Park, S. H.; Jeon, S. *Nanotechnology* **2016**, *27*, 325203.
(51) Choi, C. H.; Su, Y. W.; Lin, L. Y.; Cheng, C. C.; Chang, C. H. *RSC Adv.* **2015**, *5*, 93779.
(52) Moffitt, S. L.; Adler, A. U.; Gennett, T.; Ginley, D. S.; Perkins, J. D.; Mason, T. O. *J. Am. Ceram. Soc.* **2015**, *98*, 2099.

(53) Moffitt, S. L.; Zhu, Q.; Ma, Q.; Falduto, A. F.; Buchholz, D. B.; Chang, R. P. H.; Mason, T. O.; Medvedeva, J. E.; Marks, T. J.; Bedzyk, M. J. *Adv. Electron. Mater.* **2017**, *3*, 1700189.
(54) Park, J. H.; Yoo, Y. B.; Oh, J. Y.; Lee, J. H.; Lee, T. I.; Baik, H. K. *Appl. Phys. Express* **2014**, *7*, 051101.
(55) Hennek, J. W.; Smith, J.; Yan, A.; Kim, M. G.; Zhao, W.; Dravid, V. P.; Facchetti, A.; Marks, T. J. *J. Am. Chem. Soc.* **2013**, *135*, 10729.
(56) Nedel'ko, V. V.; Korsunskii, B. L.; Dubovitskii, F. I.; Gromova, G. L. *Polym. Sci. U.S.S.R.* **1975**, *17*, 1697.
(57) Louette, P.; Bodino, F.; Pireaux, J.-J. *Surf. Sci. Spectra* **2005**, *12*, 54.
(58) Khader, M. M.; Al-Marri, M. J.; Ali, S.; Qi, G.; Giannelis, E. P. *Am. J. Anal. Chem.* **2015**, *06*, 274.
(59) Haas, H. C.; Schuler, N. W.; Macdonald, Rl *J. Polym. Sci., Part A-1: Polym. Chem.* **1972**, *10*, 3143.
(60) Segut, O.; Herlem, G.; Lakard, B.; Blondeau-Patissier, V.; Nardin, M.; Gree, S.; Rauch, J. Y. *Synth. Met.* **2010**, *160*, 1359.
(61) Kasten, L. S.; Grant, J. T.; Grebasch, N.; Voevodin, N.; Arnold, F. E.; Donley, M. S. *Surf. Coat. Technol.* **2001**, *140*, 11.
(62) Zou, G. F.; Zhao, J.; Luo, H. M.; McCleskey, T. M.; Burrell, A. K.; Jia, Q. X. *Chem. Soc. Rev.* **2013**, *42*, 439.
(63) Jia, Q. X.; McCleskey, T. M.; Burrell, A. K.; Lin, Y.; Collis, G. E.; Wang, H.; Li, A. D.; Foltyn, S. R. *Nat. Mater.* **2004**, *3*, 529.
(64) Evmenenko, G.; Fister, T. T.; Buchholz, D. B.; Li, Q.; Chen, K. S.; Wu, J.; Dravid, V. P.; Hersam, M. C.; Fenter, P.; Bedzyk, M. J. *ACS Appl. Mater. Interfaces* **2016**, *8*, 19979.
(65) Buchholz, D. B.; Zeng, L.; Bedzyk, M. J.; Chang, R. P. H. *Prog. Nat. Sci.* **2013**, *23*, 475.
(66) Labram, J. G.; Treat, N. D.; Lin, Y. H.; Burgess, C. H.; McLachlan, M. A.; Anthopoulos, T. D. *Adv. Funct. Mater.* **2016**, *26*, 1656.
(67) Woods, K. N.; Thomas, M. C.; Mitchson, G.; Ditto, J.; Xu, C.; Kayal, D.; Frisella, K. C.; Gustafsson, T.; Garfunkel, E.; Chabal, Y. J.; Johnson, D. C.; Page, C. J. *ACS Appl. Mater. Interfaces* **2017**, *9*, 37476.
(68) Buckley, D.; McNulty, D.; Zubialevich, V.; Parbrook, P.; O'Dwyer, C. *J. Vac. Sci. Technol., A* **2017**, *35*, 061517.
(69) Tomai, S.; Terai, K.; Junke, T.; Tsuruma, Y.; Ebata, K.; Yano, K.; Uraoka, Y. *J. Appl. Phys.* **2014**, *115*, 083701.
(70) Kuznetsov, V. L.; O'Neil, D. H.; Pepper, M.; Edwards, P. P. *Appl. Phys. Lett.* **2010**, *97*, 262117.
(71) Buchholz, D. B.; Ma, Q.; Alducin, D.; Ponce, A.; Jose-Yacaman, M.; Khanal, R.; Medvedeva, J. E.; Chang, R. P. *Chem. Mater.* **2014**, *26*, 5401.
(72) Leenheer, A. J.; Perkins, J. D.; van Hest, M. F. A. M.; Berry, J. J.; O'Hayre, R. P.; Ginley, D. S. *Phys. Rev. B: Condens. Matter Mater. Phys.* **2008**, *77*, 115215.
(73) Medvedeva, J. E. *EPL* **2007**, *78*, 57004.
(74) Zhou, N.; Kim, M. G.; Loser, S.; Smith, J.; Yoshida, H.; Guo, X.; Song, C.; Jin, H.; Chen, Z.; Yoon, S. M.; Freeman, A. J.; Chang, R. P.; Facchetti, A.; Marks, T. J. *Proc. Natl. Acad. Sci. U. S. A.* **2015**, *112*, 7897.
(75) Yeh, T. C.; Zhu, Q.; Buchholz, D. B.; Martinson, A. B.; Chang, R. P. H.; Mason, T. O. *Appl. Surf. Sci.* **2015**, *330*, 405.
(76) Medvedeva, J. E.; Buchholz, D. B.; Chang, R. P. H. *Adv. Electron. Mater.* **2017**, *3*, 1700082.
(77) Zhou, Y. H.; Fuentes-Hernandez, C.; Shim, J.; Meyer, J.; Giordano, A. J.; Li, H.; Winget, P.; Papadopoulos, T.; Cheun, H.; Kim, J.; Fenoll, M.; Dindar, A.; Haske, W.; Najafabadi, E.; Khan, T. M.; Sojoudi, H.; Barlow, S.; Graham, S.; Bredas, J. L.; Marder, S. R.; Kahn, A.; Kippelen, B. *Science* **2012**, *336*, 327.
(78) Sun, B.; Hong, W.; Thibau, E.; Aziz, H.; Lu, Z.-H.; Li, Y. *Org. Electron.* **2014**, *15*, 3787.

DOI: 10.1021/jacs.8b01252
J. Am. Chem. Soc. 2018, 140, 5457−5473